# Optimisation of Filter Compositions in Boron Neutron Capture Therapy

by

S. J. Aarts

to obtain the degree of Master of Science
at the Delft University of Technology

July 10, 2019

| | |
|---|---|
| Student number: | 4275489 |
| Department: | Delft University of Technology, Faculty of Applied Sciences,<br>Department of Radiation Science and Technology |
| Thesis committee: | prof. dr. J.L. Kloosterman,<br>dr. D. Lathouwers,<br>dr. E. van der Kolk |

# Contents

# 1 Introduction

## 1.1 Boron neutron capture therapy

Boron Neutron Capture Therapy (BNCT) is a type of radiotherapy that can be used to treat various types of cancer. It is based on the nuclear reaction that occurs when neutrons are captured by the $^{10}\mathrm{B}$ isotope. This nuclide has a high capture cross section, especially for low energy neutrons (see Figure 1.1). In BNCT, the boron needs to be delivered into the patient's tumour by a biochemically targeted drug. If there is a sufficient amount of $^{10}\mathrm{B}$ atoms present in each cancer cell, one or more neutron beams are directed towards the tumour region to initiate the capture reactions. The capture reaction is illustrated in the scheme below.

$$\begin{array}{ccccccc} {}^{10}\mathrm{B} + \mathrm{n_{th}} & \longrightarrow & [{}^{11}\mathrm{B}] & \longrightarrow & {}^{4}\mathrm{He} + {}^{7}\,\mathrm{Li} & \qquad & (Q = 2.79\ \mathrm{MeV}) \\ &&&& \downarrow (94\%) && \\ &&&& \gamma && \end{array}$$

In this reaction, a total energy of 2.79 MeV is released. This energy is distributed over the emitted alpha particle (1.47 MeV) and the recoiling $^{7}\mathrm{Li}$ ion (1.32 MeV). In 94% of all cases, a 0.48 MeV gamma is emitted as well [1]. Both the alpha particle and $^{7}\mathrm{Li}$ ion have high linear energy transfer (LET) characteristics, which means they deposit their energy over a relatively small range. In human tissue, the track lengths of these particles are on average 8.9 $\mu$m for $^{4}\mathrm{He}$ and 4.8 $\mu$m for $^{7}\mathrm{Li}$ [2]. This is comparable to the diameter of a single cell. Hence, all their energy is deposited within the targeted cell. This way, it is possible to selectively kill cancer cells, while healthy cells are spared if these have not taken up high amounts of boron. A high tumour-to-healthy tissue ratio in boron concentration is therefore essential for the effectiveness of BNCT.

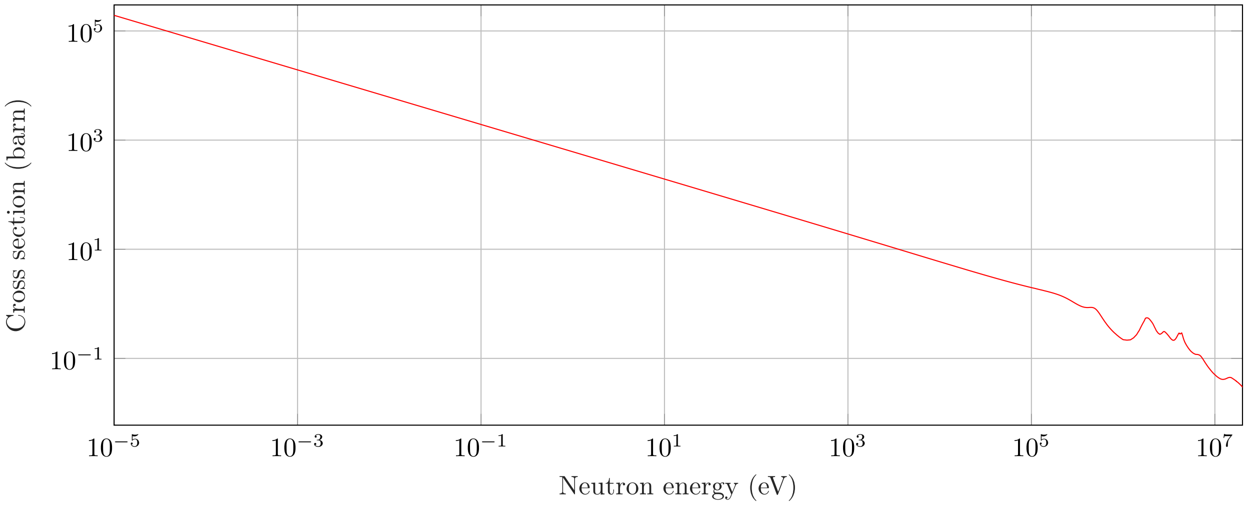

**Figure 1.1:** Microscopic $(n, \alpha)$ cross section for B-10 as a function of neutron energy [3].

## 1.2 Short history of BNCT

The idea to apply the boron capture reaction in radiation therapy was first proposed by Locher [4] in 1936. Soon after his suggestion the first experiments in cell cultures and mice started. In the early 1940s, Kruger [5] and Zahl [6] demonstrated that BNCT worked as suggested. From this point on, interest primarily developed in treating high-grade brain tumours (glioblastoma multiforme), a malignant type of cancer that is usually fatal within six months of diagnosis [7]. It was reasoned that the reduction of the blood brain barrier at the tumour could be exploited to selectively increase the concentration of boron in the cancer cells [8].

In the early 1950s, the first clinical trials on BNCT took place at Brookhaven National Laboratory (BNL) in the United States. Ten patients suffering from glioblastoma multiforme were irradiated by thermal neutrons after a $^{10}$B-enriched borax solution was injected [9]. Around the same time, comparable trials were performed at Massachusetts Institute of Technology (MIT). The outcomes and average survival time after BNCT did not show any improvement compared to conventional therapies [9, 10]. The overall results of the trials at BNL and MIT were considered unsatisfactory. It was concluded that thermal neutrons do not penetrate deep enough and that the boron compounds were not sufficiently selective [11]. As a consequence, research on BNCT came to an end around 1961 in the United States.

Despite the poor results, Hatanaka [10] introduced new clinical trials in Japan starting from 1968. Over 120 patients were treated and there have been reports of excellent clinical results in some malignant glioma patients [9]. The success was mainly due to the availability of some new boron compounds: sodium borocaptate (BSH) was synthesised by Soloway [12] and later also p-boronophenylalanine (BPA) was used by Mishima [13]. At this stage, the first steps were taken to apply BNCT on other types of cancer such as skin melanoma and head and neck cancer.

After the promising results in Japan, other researchers regained interest in BNCT and both BNL and MIT started new trials in the 1990s. At the beginning of this century, trials were started in the Netherlands (Petten, 2002), Finland (2003), Sweden (2003), the Czech Republic (2002), again in Japan (2003), Argentina (2004) and Taiwan (2004) [14]. All mentioned studies were carried out at research reactor facilities and applied epithermal neutron beams to increase the penetration depth of neutrons into tissue. Several encouraging outcomes have been reported about these trials. The Finish group, for instance, has reported increased survival times of patients with glioblastoma multiforme that were treated with BNCT [15]. Meanwhile, many of these BNCT programs have been brought to an end.

## 1.3 Current status and challenges

Even after many decades of research, BNCT is still considered as an experimental treatment. There are several problems that need to be solved before BNCT could become a serious alternative for current cancer treatments such as proton therapy. First of all, there is the need for more selective boron compounds. The two boron compounds that were discovered in the 1960s are nowadays still the only available options [14]. Some research is aimed at finding new methods to enhance the uptake and retention of the existing boron compounds. Other research is focused on finding new boron compounds. These should be non-toxic with a tumour-to-normal tissue ratio greater than 3 [16]. Whenever a new compound is proposed, there is still a long and expensive procedure needed to investigate and approve the drug before it can be used in clinical practice. Nevertheless, there are some promising candidates under development [17]. In recent years, nano-sized particles are becoming an increased topic of interest. The use of liposomes and nanoparticles could make it possible to perform controlled and sustained release of boron in the tumour cells. These nanoscale delivery systems have already shown some promising results [18].

Secondly, the availability of effective neutron sources is of importance. Until now, all BNCT trials have been performed at thermal research reactors. At these facilities it is possible to generate high intensity neutron beams that have been essential for the development of BNCT. However, the use of nuclear reactors has some drawbacks. Usually, research reactors are used for many other applications. This can lead to conflicts or limitations in the BNCT work. Additionally, most reactors are separated from hospitals, which causes some logistic difficulties in performing clinical trials. As an alternative, it has been proposed to use accelerator-based neutron sources. These sources are more compact and less expensive than nuclear reactors. They can be placed in hospitals and the required licensing procedure is much easier. In accelerator-based sources, a beam of charged particles is produced and directed at a target that releases neutrons after impact. The source strength of the produced neutron beam is generally low compared to reactor sources. In many types of accelerators, an increase in intensity of the resulting neutron beam by more than an order of magnitude is needed [14]. Several reviews have reported that this required increase appears to be possible [19].

Finally, some other practical reasons are mentioned as obstacles in the current development of BNCT. The implementation of this treatment requires collaboration between very different disciplines such as nuclear physics, chemistry, surgery and radiation biology. In treatment planning, knowledge from all these research fields needs to be combined. Several systems for treatment planning have been developed in recent years [2]. For further development, large-scale clinical trials need to be performed, which can only be realized if a sufficient number of BNCT facilities becomes available in hospital environments.

## 1.4 The scope of this thesis

This thesis is focused on the design of neutron filters. In BNCT, a neutron filter is placed between the neutron source and the patient to tailor the spectrum. A standard neutron filter consists of a series of layers of various materials which are positioned perpendicular to the incident neutron beam (see Figure 1.2). The incoming neutrons interact with the materials inside the filter. Various reactions can occur depending on the material properties. The most important interactions are:

- **Elastic scattering** $(n, n)$: the neutron simply scatters off the nucleus causing a change in energy and direction of the neutron. Kinetic energy is conserved in this event.
- **Inelastic scattering** $(n, n')$: the neutron scatters off the nucleus while leaving it in an excited state. The neutron may lose a large amount of energy because of the the threshold energy that is needed to excite the nucleus. The unstable nucleus returns to its ground state by emitting some type of radiation, often a gamma ray. Kinetic energy is not conserved in inelastic collisions.
- **Radiative capture** $(n, \gamma)$: the neutron is absorbed by the nucleus to form a new compound nucleus in an excited state. This nucleus decays to its ground state by emitting a gamma ray.
- **Other absorption reactions** such as $(n, p)$ and $(n, \alpha)$: the neutron is absorbed by the nucleus followed by the emission of another particle such as a proton or alpha particle.

As a result, the neutrons leaving the filter will have a modified spectrum.

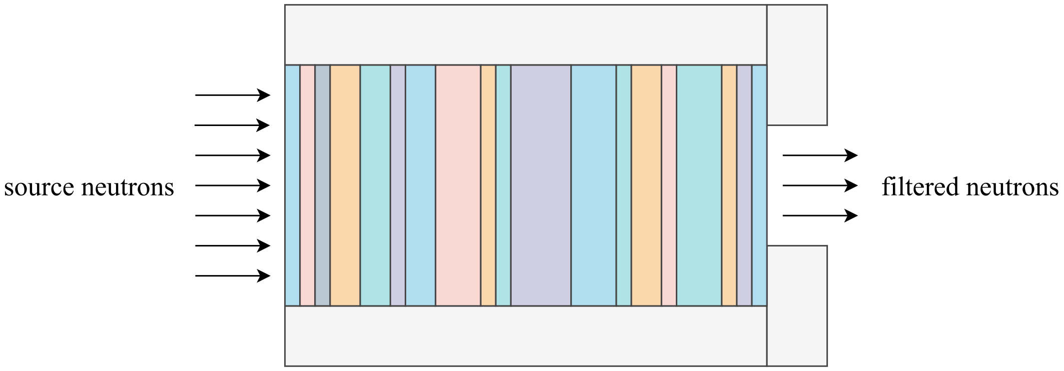

**Figure 1.2:** Standard design of a multi-layered neutron filter. The incoming neutrons interact with the nuclei of the filters materials by (in)elastic scattering and absorption. Part of the neutrons is leaving the filter through the final collimator. The neutron filter is designed in such a way that the output spectrum is optimised to treat the patient.

The purpose of this work is to develop algorithms that are able to optimise the neutron filter compositions in BNCT. This is done by choosing the filter materials and thicknesses in such a way that an optimal neutron beam is created to treat the patient. In order to develop these optimisation methods, calculation schemes are needed to model neutron transport and to estimate the resulting dose contributions inside the patient. Furthermore, the possibilities are investigated to set up an effective treatment plan based on the optimised neutron filters. An additional goal is to gain more insight in possible limitations that still exist in BNCT treatments. This might involve the $^{10}$B uptake ratio between the tumour and healthy tissue for instance.

The remainder of this thesis is organized as follows. In Chapter 2, some basic principles about neutron filtering are discussed. It is explained which requirements an optimal neutron beam should meet. Also, a selection of useful filter materials is made to be used in the optimisations. Before these optimisations are performed, a better understanding about neutron and photon transport is needed. A distinction is made between particle transport inside the filter (Chapter 3) and inside the patient (Chapter 4). A deterministic method is used to model neutron transport inside the filter. Here, the discrete ordinates method is explained and several tools are investigated to reduce computation time. Particle transport inside the patient is modelled by a Monte Carlo code. In this chapter, the most important dose components are described and it is explained how these dose components can be estimated. After this, the filter optimisation problem is worked out for a specific situation. This involves a simplified case of a brain tumour patient that is treated with BNCT. The details of this model problem are described in Chapter 5. Two different types of algorithms are used to address the model problem. In Chapter 6, an optimisation method based on gradient descent is elaborated. The other approach includes a genetic algorithm, which is described in Chapter 7. The resulting filter compositions and dose distributions are discussed for both optimisation methods. Finally, some conclusions and recommendations are given in Chapter 8.

# 2 | Neutron Filter Design

## 2.1 General beam requirements

In practice, there is a large variety of factors to take into account to determine the optimal beam characteristics in treatment planning, such as the shape and location of the tumour, possible metastasis, organs at risk and the local boron distribution in tissues. Some of these features are discussed in further chapters. At this point it is useful to zoom out a little and discuss some general beam requirements that can serve as a guideline for selecting filter materials.

### 2.1.1 Neutron energy

We can distinguish between thermal, epithermal and fast neutrons based on the kinetic energy. Different boundaries of these energy ranges are found in literature. In this thesis, the common definition from the International Atomic Energy Agency (IAEA) [8] is applied:

| | |
|---|---|
| Thermal neutrons: | $E < 0.5$ eV |
| Epithermal neutrons: | $0.5$ eV $< E < 10$ keV |
| Fast neutrons: | $E > 10$ keV |

Thermal neutrons are the most important for BNCT because they have the largest probability to be captured in boron. They have been used in early trials, but did not give optimal results. The thermal neutron flux decreases strongly as a function of tissue depth, primarily because they are captured by hydrogen atoms. Also, it is difficult to collimate the neutron beam and restrict its range to the tumour region because of thermal neutron scattering. For these reasons, the use of thermal neutron beams often leads to insufficient penetration in tissue, which makes it impossible to treat deep tumours.

These limitations can be solved by using higher-energy neutrons. When epithermal neutrons enter tissue, they are moderated by collisions with mostly hydrogen atoms before they are captured by boron nuclei. This way, epithermal neutrons can penetrate the tissue while protecting the skin from severe damage by high-LET radiation. Figure 2.1 shows a comparison between a thermal and epithermal neutron beam entering soft tissue. If we extend this reasoning, one could argue to use fast neutrons for treating even deeper located tumours. Unfortunately, fast neutrons will cause an additional dose component by recoil protons through collisions with hydrogen nuclei. These high-LET protons mostly damage the upper surface and skin tissue, which makes fast neutrons undesirable when treating deep tumours. This effect is described in more detail in Section 4.2 of this thesis.

These considerations resulted in the current trend to use only epithermal neutron beams for clinical therapy in BNCT. This objective is challenging because it concerns an energy level between thermal and fast energies, which are both undesirable. It is complicated to reduce thermal and fast spectrum contributions without affecting the epithermal component too much. Any filter material that is able to decrease the fast neutron component will decrease the epithermal neutron component to some extend as well.

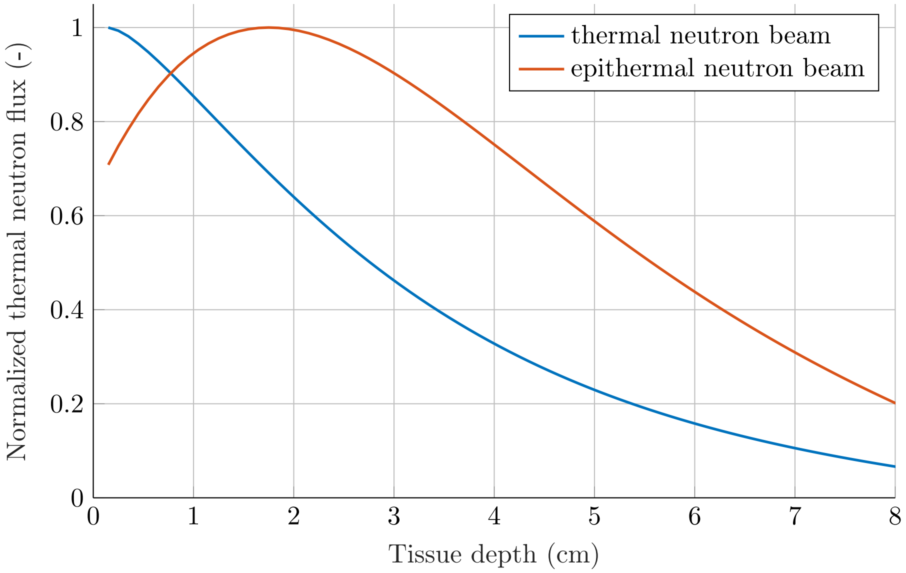

**Figure 2.1:** Comparison of the thermal neutron flux for thermal and epithermal neutron beams entering soft tissue. These fluxes have been calculated by a one-dimensional discrete ordinates code (XSDRN). The use of this code is explained in Chapter 3 of this thesis. The tissue is modelled using a standard atomic composition from the International Commission on Radiation Units and Measurements (ICRU) [20].

### 2.1.2 Gamma ray component

Other types of radiation such as gamma rays can contaminate the neutron beam. Gammas are either emitted directly from the neutron source (which is the reactor core in most cases) or by $(n,\gamma)$ reactions inside the filter or patient. Gamma radiation is unwanted because it delivers a non-selective dose over a long range and this could damage a large volume of healthy tissue. Therefore, gamma radiation needs to be reduced to an acceptable level.

### 2.1.3 Current-to-flux ratio

The neutron current-to-flux ratio is a measure of the fraction of neutrons that is moving in the forward direction. A high value of this ratio is desirable because it ensures that the neutron beam is focused towards the tumour region and prevents divergence to adjacent healthy tissues. In addition, a forwardly-peaked beam offers flexibility to position the patient along the beam axis. If necessary, the patient can be placed a little further away from the beam port without a big loss in neutron flux. The current-to-flux ratio is affected by neutron scattering inside the filter. Unwanted beam directions can be blocked by using a collimator at the cost of reducing the total neutron flux somewhat.

### 2.1.4 Beam intensity

The neutron flux needs to be high enough to initiate a sufficient amount of $^{10}B(n,\alpha)^{7}Li$ reactions to kill the tumour cells within a reasonable time. Beam intensity and treatment time are directly connected; a lower beam intensity can be compensated by irradiating the patient for a longer time. However, long irradiation times are undesirable for the comfort of the patient and the effectiveness of the treatment. During the entire treatment, the $^{10}B$ concentration in the tumour needs to be maintained at a specific level, which may not be possible for a long time. The IAEA applies a maximum treatment time of one hour and concludes from experience that a desirable minimum beam intensity would be $10^9$ epithermal neutrons $cm^{-2}s^{-1}$ [8]. In addition, fractionation can be considered as an alternative to avoid extremely long treatment times.

## 2.2 Material selection

The next step in the design process is to make a selection of materials with useful properties to use in the filter. These materials can be classified into different categories depending on the function they have. The main filter components are spectrum shifters, thermal neutron absorbers and gamma shields. These components can be built up by multiple layers of various materials. Additionally, the filter consists of radial components to reflect and collimate neutrons. In this section, each component is discussed and some suitable materials are recommended. This material selection is partly based on recommendations from other filter optimisation studies performed by Hassanein [21], Ross [22], Tracz [23] and Azahra [24]. The suitability of materials depends primarily on the nuclear cross section, which is a measure of the interaction probability for neutrons. Therefore, nuclear cross section data from the Evaluated Nuclear Data Library [3] is used to support the choice of materials.

### 2.2.1 Spectrum shifters

The function of the spectrum shifters is to moderate fast neutrons to the epithermal range. For this purpose, high scattering cross sections are required for fast neutrons, while cross sections below 10 keV should be relatively low. This way, high-energy neutrons lose part of their energy by scattering and ideally end up in the epithermal range. High scattering cross sections for fast neutrons normally appear in the form of narrow resonance peaks. This means that a single material is not capable of moderating fast neutrons over the full range. As a consequence, it is always necessary to use several spectrum shifter materials and combine multiple resonance peaks to cover the fast neutron range completely.

Some elements with suitable scattering cross sections are $^4$He, $^7$Li, $^{19}$F and $^{27}$Al. In order to compare their cross sections effectively, we can define the relative scattering cross section

$$R(E) = \frac{\sigma(E)}{\sigma_{epi}}. \tag{2.1}$$

Here, the scattering cross section $\sigma(E)$ is normalized by $\sigma_{epi}$, which is the average epithermal cross section:

$$\sigma_{epi} = \frac{1}{E_2 - E_1} \int_{E_1}^{E_2} \sigma(E) dE, \tag{2.2}$$

where $E_1$ and $E_2$ are the lower and upper boundary of the epithermal interval. This way, the cross sections are scaled with respect to $\sigma_{epi}$ (see Figure 2.2).

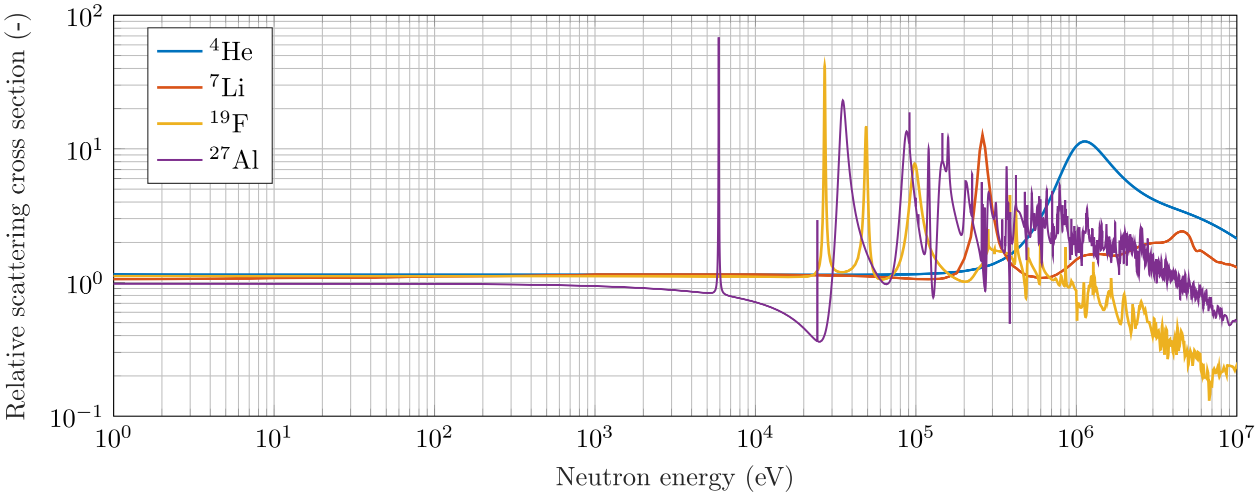

**Figure 2.2:** Relative scattering cross section $R(E)$ for various nuclides.

A combination of these four nuclides is already capable of moderating a substantial amount of neutrons above 20 keV. This example also shows the importance of the order of the filter materials; there is a logical sequence of layers starting with materials which can scatter high-energy neutrons towards materials with resonance peaks at lower energies. Other nuclides that can be used as spectrum shifter are $^{16}$O, $^{24}$Mg, $^{28}$Si, $^{32}$S, $^{40}$Ar, $^{46}$Ti and $^{60}$Ni. Some of the selected nuclides can be used individually (most metals for example). Others are combined in molecular bindings such as $AlF_3$ and LiF.

The material selection is not only based on the scattering properties. Some other desired characteristics are:

- **Low absorption cross section**: the beam intensity needs to be high enough for a successful treatment. Therefore, the absorption of both epithermal and fast neutrons should be minimal.
- **Low mass number**: light elements are generally better moderators. In elastic scattering, the maximum possible energy loss per collision is higher for low atomic masses. Moreover, it is possible to maintain a stronger forwardly-peaked beam direction if less scattering has occurred. Therefore, most of the selected candidate nuclides have low mass numbers of $A \leq 32$. Since it is unclear how strong this effect will be exactly, some heavier nuclides (e.g. $^{60}$Ni) are included as well because of other useful properties.
- **Low gamma production**: gamma radiation is delivering a non-specific dose and is therefore considered as a contaminating beam component. Gamma rays can be emitted by capture reactions, so materials with low $(\mathrm{n}, \gamma)$ cross sections are preferred.

### 2.2.2 Thermal neutron absorbers

The most commonly used materials for thermal neutron absorbers are cadmium and boron. Natural cadmium consists of eight isotopes including $^{113}$Cd which gives rise to the desired properties. Figure 2.3 shows the total neutron cross section of $^{113}$Cd. There is a sharp transition around 0.5 eV with the result of thermal neutrons being absorbed without a large effect on epithermal neutrons. The main drawback of cadmium is the emission of gamma rays that follows after thermal neutron absorption. Gammas are emitted at various characteristic energy levels up to 2.46 MeV, among which the most frequent is a 0.56 MeV gamma that is emitted in 85% of all neutron absorptions [25]. Alternative materials are being investigated because of the increasingly stricter regulations on the use of cadmium in equipment [26].

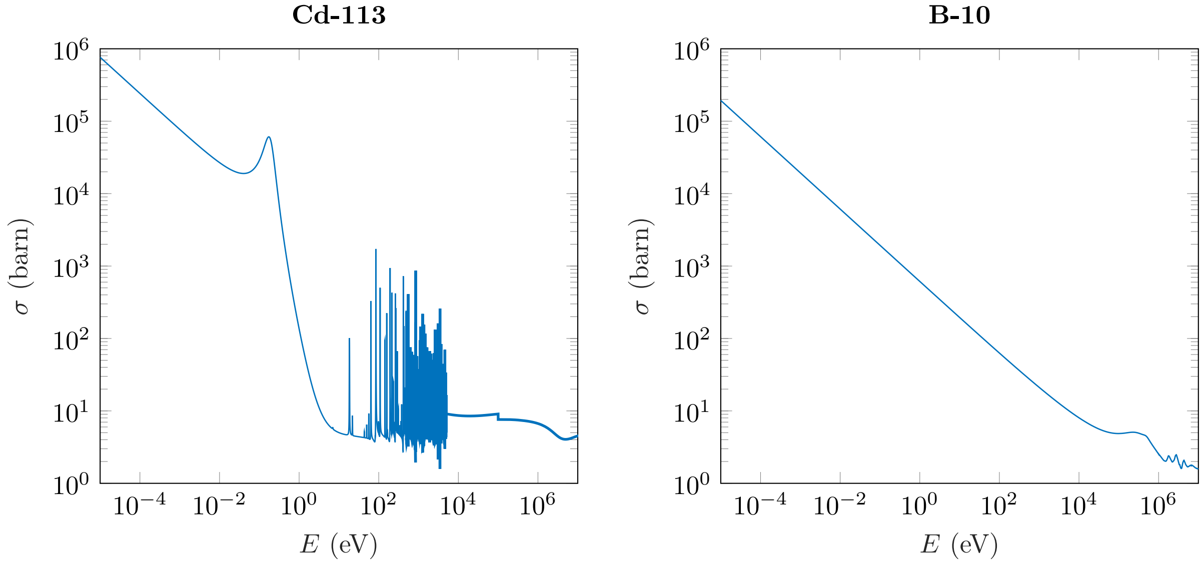

**Figure 2.3:** Total neutron cross sections of $^{113}$Cd and $^{10}$B. It can be seen that cadmium is more selective in absorbing thermal neutrons than boron.

Boron can also be used as a thermal neutron absorber. $^{10}$B is useful for the same reason as it is used in BNCT: because of its large thermal neutron cross section by the (n,$\alpha$) capture reaction. Instead of a distinct transition, $^{10}$B is showing a $1/v$ dependence over the full energy range (Figure 2.3). This makes boron a less selective material. The neutron capture reaction in $^{10}$B produces a 0.48 MeV gamma in 94% of all cases [1]. This gamma ray is somewhat less energetic than the gamma emissions in cadmium. Boron is also attractive because of its low cost in comparison to other materials [26]. It is normally used in the form of boron carbide sheets ($B_4C$). For both boron and cadmium, only thin layers are needed to construct a thermal neutron absorber; no more than a few millimeters are sufficient to remove the complete thermal neutron spectrum in most cases.

### 2.2.3 Gamma shields

Suppose a collimated beam of mono-energetic photons with intensity $I_0$ is travelling through a layer of a material with mass density $\rho$. The intensity inside the slab can be described by an exponential absorption law: after a distance $x$, the beam intensity has decreased to $I(x) = I_0 e^{-\mu \cdot x}$. The quantity $\mu/\rho$ is defined as the mass attenuation coefficient. This measure of the gamma attenuation can be determined experimentally. The value depends on the sum of the probabilities of the possible photon interactions, which are (in)coherent scattering, the photo-electric effect and pair production [27]. Materials with favourable mass attenuation coefficients are glass systems consisting of lead (Pb) and bismuth (Bi) [28]. These materials are suitable for gamma shielding. In our application, it is also important to sustain the neutron flux. Both Pb and Bi are relatively transparent to neutrons. There is a small preference for bismuth, since it is nearly as good as lead for shielding gamma rays, while having a higher transmission of epithermal neutrons [8]. The transmission rates for both materials are compared in Figure 2.4.

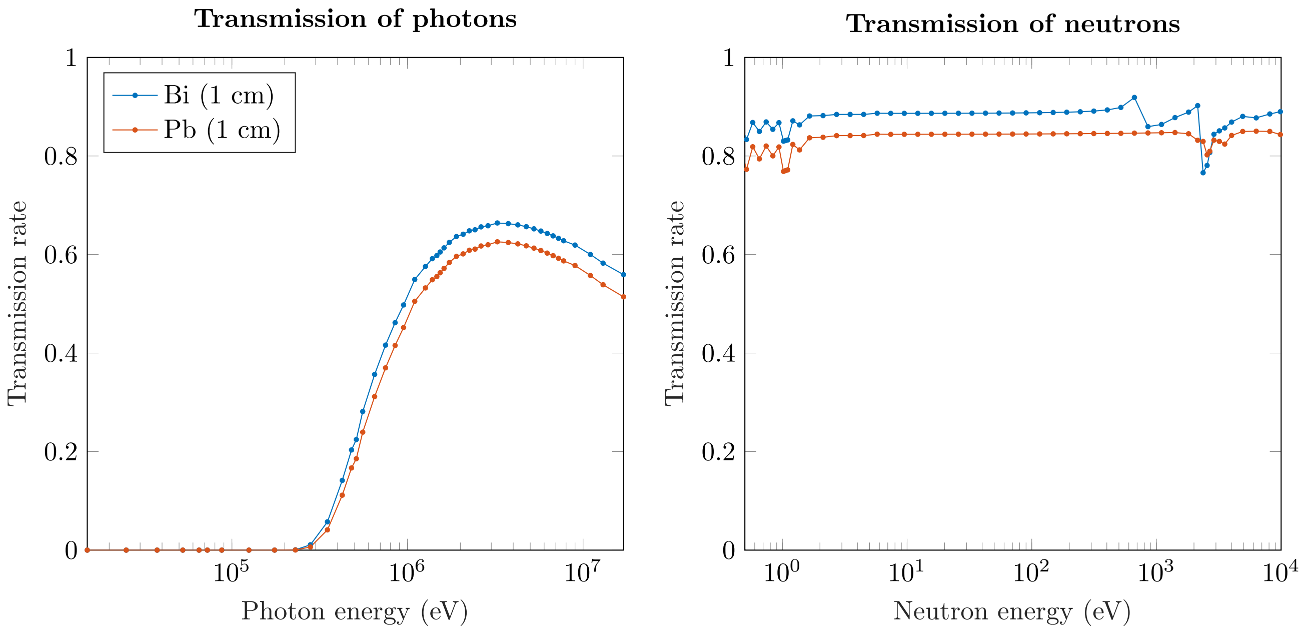

**Figure 2.4:** Transmissions rates for photons and epithermal neutrons in 1 cm thick slabs of bismuth and lead. The values have been calculated by the one-dimensional discrete ordinates code XSDRN. A detailed explanation about these calculations is given in Chapter 3. Most of the lower-energy photons are absorbed in the 1 cm slabs, while photons with energies higher than 300 keV require thicker gamma shields to be removed. For epithermal neutrons, bismuth has a somewhat higher transmission than lead.

### 2.2.4 Radial components

The radial components are placed around the main filter layers. Reflectors and collimators are supposed to reflect neutrons back into the beam. This can be achieved by using materials with high scattering cross sections and high atomic masses for a minimum energy loss per collision. Lead, bismuth and lead fluoride are useful for this reason [21]. The collimators close to the beam port are beam delimiters and should absorb neutrons to prevent them leaving the filter system at undesired angles. These collimators are usually made of $B_4C$ or $Li_2CO_3$ dispersed in polyethylene [8]. Outside the entire system, a high-density concrete shield should be placed to protect the environment from all types of radiation. The concrete shield can be mixed with iron minerals to increase the gamma absorption even further.

The risk of activations inside the neutron filter should also be taken into account in the material selection. This applies for all components mentioned before. Some materials might accumulate long-term radioactivity or toxic substances after neutron activation occurred. This is the case for bismuth for example. After a neutron is captured by $^{209}$Bi, the highly radioactive $^{210}$Po is created in combination with beta decay. Polonium is an extremely dangerous alpha emitter that can already be lethal in tiny amounts [29]. Therefore, caution is needed with respect to neutron activation inside the filter. Materials like bismuth should either be avoided or encapsulated.

# 3 | Neutron and Gamma Transport

## 3.1 The Boltzmann transport equation

A complete description of the neutron field inside the filter is given by the angular neutron flux $\varphi(\vec{r}, E, \hat{\Omega}, t)$. In general, this quantity depends on seven independent variables, which are the position $\vec{r} = \langle x, y, z \rangle$, angular direction $\hat{\Omega} = \langle \theta, \phi \rangle$, energy $E$ and time $t$. The angular flux can be obtained by solving the Boltzmann transport equation. This equation is given by [30]:

$$\frac{1}{v}\frac{\partial \varphi}{\partial t} + \hat{\Omega} \cdot \nabla \varphi + \Sigma_t(\vec{r}, E)\varphi(\vec{r}, E, \hat{\Omega}, t) = \int_{4\pi} d\hat{\Omega}' \int_0^\infty dE' \Sigma_s(E' \to E, \hat{\Omega}' \to \hat{\Omega})\varphi(\vec{r}, E', \hat{\Omega}', t) + S(\vec{r}, E, \hat{\Omega}, t). \tag{3.1}$$

The Boltzmann transport equation follows directly from balancing the various mechanisms by which neutrons can be gained or lost in a system. Losses are due to leakage (second term) and collisions (third term). Both absorption and scattering (causing a change in $E$ and/or $\hat{\Omega}$) account for a loss of neutrons with this specific energy and direction. Therefore, the total neutron cross section $\Sigma_t$ is used here. Gain mechanisms are inscattering (fourth term) and any other neutron source (fifth term). Inscattering is the event of neutrons with a different $E'$ and $\hat{\Omega}'$ suffering a scattering collision that changes their energy and direction into the $E$ and $\hat{\Omega}$ of interest. The difference between all gains and losses is equal to the rate of change of the angular neutron flux (first term).

In many cases the general transport equation can be simplified somewhat. For our neutron filter model, it is convenient to use a one-dimensional slab geometry as shown in Figure 3.1. This means the neutron flux only depends on a single spatial coordinate, say $x$. The direction $\hat{\Omega}$ is given by $\theta$ which is the angle with the positive x-axis. Also, the assumption is made that a stationary situation has been reached inside the system. Hence, the model is time-independent.

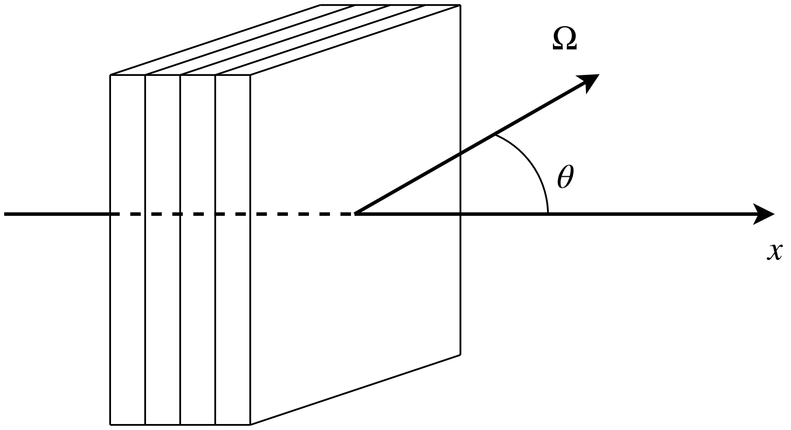

**Figure 3.1:** Coordinate system of the one-dimensional slab geometry in which the filter layers are placed perpendicular to the x-axis. The direction in which the neutrons are moving is given by the angle $\theta$.

These simplifications reduce the number of independent variables from seven to three. The new transport equation becomes

$$\mu\frac{\partial\varphi}{\partial x}+\Sigma_t(x,E)\varphi(x,E,\mu)=\int_{-1}^{+1}d\mu'\int_0^{\infty}dE'\Sigma_s(E'\to E,\mu'\to\mu)\varphi(x,E',\mu')+S(x,E,\mu), \tag{3.2}$$

with $\mu=\cos\theta$. It is hardly ever possible to solve this equation analytically. Therefore, other methods are used to approximate the solution.

## 3.2 The discrete ordinates method

It was decided to use a deterministic method to solve the simplified Boltzmann transport equation. In this approach, all continuous variables in the equation are replaced by a discrete set of values. Similarly, all operations are replaced by their discretized counterparts. Derivatives can be represented by finite difference formulas and integrals by numerical quadrature formulas. This way, one arrives at a set of algebraic equations for the discrete representation of $\varphi$. This approach is called the discrete ordinates method or $S_N$ method and can be used to solve the Boltzmann transport equation numerically. In our case, the one-dimensional discrete ordinates code XSDRN is used. This routine is part of the SCALE Code System [31].

### 3.2.1 Discretizing the variables

All three independent variables ($E$, $x$ and $\mu$) need to be discretized. The neutron energy $E$ spans a wide range from $10^{-5}$ eV up to 20 MeV. This full energy range can be divided into intervals or so-called energy groups. In our XSDRN calculation, a standard library of 200 neutron energy groups is used. The spacing between the energy groups is approximately logarithmic with a somewhat finer structure in the resonance regions. In these regions, both cross sections and the neutron flux can vary strongly with energy.

The position variable $x$ is decomposed into a spatial mesh. Inside the neutron filter, different mesh sizes are chosen depending on the material. Some materials (e.g. aluminium) have only weak interactions with neutrons and can be modelled in a relatively course spatial mesh. Other materials require a finer mesh, because they are strong neutron absorbers (e.g. cadmium). Therefore, the mesh size is taken inversely proportional to the total macroscopic neutron cross section $\Sigma_t$ of the material of interest.

Finally, the angular variable $\mu$ is defined as a set of discrete directions and corresponding weights. This way, the integral $\int_{-1}^{+1}f(\mu)d\mu$ can be replaced by the sum $\sum_{m=1}^{M}w_m f(\mu_m)$. The quadrature points $(\mu_m,w_m)$ need to be chosen is such a way that functions can be integrated with maximum accuracy. A double Gauss-Legendre quadrature set of order 16 is selected based on recommendations from Carlson [32].

### 3.2.2 Calculation of the group cross sections

The discretization of the problem also affects the cross sections in the transport equation. Instead of continuously defined functions $\Sigma(E)$, so-called group cross sections $\Sigma_g$ are defined which have constant values within each energy group $g$. The group cross sections are supposed to have values that preserve the reaction rates that would arise from integrating the continuous cross section by group. The problem is that the neutron flux $\varphi(E)$ appears in their formal definition, while $\varphi(E)$ is of course unknown beforehand. To solve this, the neutron flux can be approximated by a weighting function $W(E)$. In our case, the group cross sections are calculated by CSASI which is another module in SCALE. For a fine group structure, the cross sections and hence the flux tend to be smoothly varying within most energy groups. In the fast energy region however, the cross sections can vary strongly due to resonances, even within a single energy group. Therefore, another module called CENTRM is used to process the cross section data in the resolved resonance regions. CSASI uses the standard weighting function $W(E)$ that is given in Table 3.1. This function roughly resembles the neutron spectrum inside a thermal reactor. Here, the spatial and angular dependence are neglected. The total group cross sections then become

$$\Sigma_{t,g} = \frac{\displaystyle\int_g \Sigma_t(E)W(E)dE}{\displaystyle\int_g W(E)dE}. \tag{3.3}$$

**Table 3.1:** Standard weighting function for processing multigroup data in CSASI [33]

| **Neutron energy $E$** | | | **Weighting function $W(E)$** |
|---|---|---|---|
| $10^{-5}$ eV | - | 0.1 eV | Maxwellian (peak at 0.025 eV) |
| 0.1 eV | - | 80 keV | $1/E$ dependence |
| 80 keV | - | 10 MeV | Watt fission spectrum ($kT = 1.273$ MeV) |
| 10 MeV | - | 20 MeV | $1/E$ dependence |

The other cross section that is present in the Boltzmann equation is $\Sigma_s(E' \to E, \mu' \to \mu)$ in the inscattering term. Again, the continuous variable $E$ is replaced by discrete groups. The change in direction from $\mu'$ to $\mu$ is indicated by a single variable $\mu_0 = \hat{\Omega}' \cdot \hat{\Omega}$. Now, the angular dependent scattering cross section can be expanded in spherical harmonics. In one dimension, these are Legendre polynomials $P_\ell(\mu_0)$. An approximation of the group-to-group scattering cross section then becomes

$$\Sigma_s(g' \to g, \mu_0) = \sum_{\ell=0}^{L} \frac{2\ell+1}{2} \Sigma_{s,\ell}(g' \to g) P_\ell(\mu_0), \tag{3.4}$$

where $\Sigma_{s,\ell}(g' \to g)$ are the tabulated angular components of the differential scattering cross section [33]. A fifth order approximation is used in XSDRN ($L = 5$).

### 3.2.3 Transport calculation in XSDRN

After discretization and calculation of the group cross sections, the so-called $S_N$ equations are formulated:

$$\mu_m \frac{\varphi_{g,i+\frac{1}{2},m} - \varphi_{g,i-\frac{1}{2},m}}{x_{i+\frac{1}{2}} - x_{i-\frac{1}{2}}} + \Sigma_{t,g,i}\varphi_{g,i,m} = \sum_{m'=1}^{M} w_{m'} \sum_{g'=1}^{G} \Sigma_{s,i}(g' \to g, \mu_0)\varphi_{g,i,m} + S_{g,i,m}. \tag{3.5}$$

This is a coupled set of equations for the group fluxes $\varphi_{g,i,m}$ representing the neutron fluxes (units of $\mathrm{cm}^{-2}\mathrm{s}^{-1}$) in energy group $g$, at spatial interval $i$ in direction $m$. The neutron beam entering the filter is placed as a fixed surface source at the left side of the first spatial interval. A vacuum boundary condition is used at the right end of the system. XSDRN solves the equations by performing multiple loops over each of the variables. In the spatial domain, the neutron fluxes are calculated both at the boundaries and the centers of the intervals. The centered fluxes are related to the boundary fluxes by weighted diamond difference assumptions. Further details about the calculation procedure can be found in the SCALE manual [33].

One of the useful features in XSDRN is the capability to perform coupled neutron-gamma calculations. So far, all equations were discussed for neutron transport, but these are similarly applied on photons. For this purpose, a standard library from SCALE is used with 200 neutron groups (from $10^{-5}$ eV to 20 MeV) and 47 gamma groups (from 10 keV to 20 MeV). This library contains neutron cross sections ($n \to n$), gamma cross sections ($\gamma \to \gamma$) and gamma production cross sections ($n \to \gamma$). In XSDRN, gamma rays arising from neutron-induced interactions are automatically determined and included in the source term that is present in Equation 3.5. Photonuclear reactions ($\gamma \to n$) are hardly ever induced by photons with energies less than 6 MeV [34]. Therefore, these interactions are not taken into account.

## 3.3 Transport model by matrix multiplication

The transport calculations in XSDRN are relatively time-consuming and new input files need to be written for each filter configuration. To overcome these issues, a simplified model of one-dimensional particle transport has been developed. This method is an extension of the fast filter estimation from Feilzer [35] who approximated the neutron filter by a linear system. Additional work is done by including angular dependence and n-$\gamma$ interactions.

### 3.3.1 Transmission and reflection matrices for slabs

The main principle of this model is to describe the filter by predefined slabs of various materials. The thickness of each slab is taken $\Delta x \approx 1/\Sigma_t$ (at $E = 25$ meV) with a maximum of $\Delta x = 10$ cm. Each slab is described by two matrices - the transmission matrix **T** and reflection matrix **R** - which contain all interaction probabilities of particles with this slab. The elements of these matrices are defined as follows:

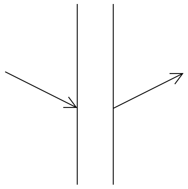

$T_{ij}$ = the expected number of particles leaving the slab on the opposite side in group $i$ per particle entering the slab in group $j$

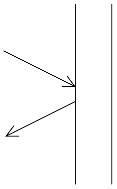

$R_{ij}$ = the expected number of particles leaving the slab on the same side in group $i$ per particle entering the slab in group $j$

Each group is specified by a particle type (neutron or gamma), energy and angular direction. The values of $T_{ij}$ and $R_{ij}$ are calculated in XSDRN. Each matrix column is the result of a single calculation for a given unit source with a specific energy and angle. The format of the XSDRN input files can be found elsewhere. Using 200 neutron energy groups, 47 gamma energy groups and 8 forward and backward angles, **T** and **R** become 1976 by 1976 matrices.

Figure 3.2 shows a part of the transmission matrices for two different materials. In these images, the matrix elements are selected that correspond to particles moving along $\mu = 0.98$ both when entering and leaving the slab. This is the most forward direction in the applied quadrature set. The majority of all particles is transmitted without a change in direction. All scattered angles give only minor contributions for a single slab. Neutron scattering becomes increasingly important when more slabs are added to expand the filter, which can be seen by a wider spread-out angular distribution of the neutron flux. Therefore, the use of angular groups and reflection matrices is necessary for an accurate estimation of the neutron spectrum at the exit of a filter.

One problem at this stage, was the appearance of a few negative values inside the transmission and reflection matrices. These are non-physical values, since the angular flux is positive by definition. It is expected that these negative fluxes are due to extrapolation errors in XSDRN. Some scattering angles are extremely unlikely to appear in the output flux for a given input angle. These group fluxes are expected to be very close to zero, but can be estimated just below zero if the spatial mesh is not fine enough. For this reason, the number of spatial intervals was increased from 20 to 100 in each slab. Although fewer negative fluxes were observed, the problem was not solved entirely by this adjustment. The remainder of the negative fluxes is set to zero to ensure a physical solution. As an alternative, a Monte Carlo code could be used to calculate the group fluxes and solve this issue completely.

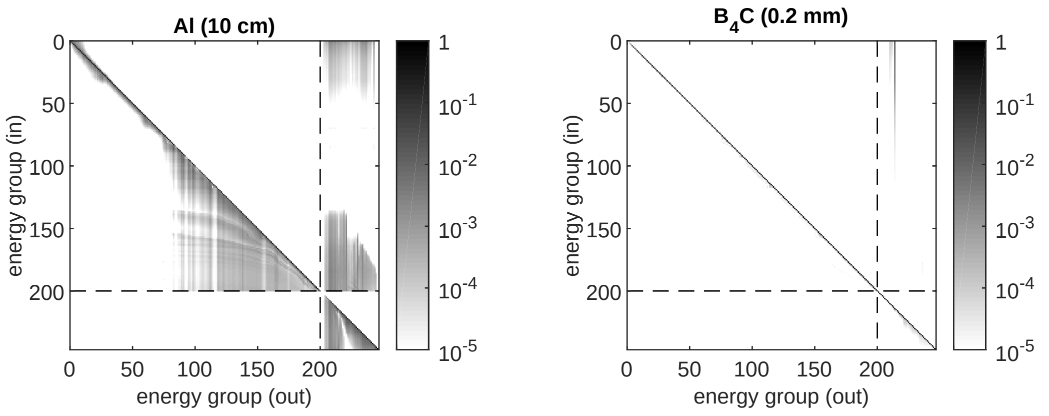
Al (10 cm)

B$_4$C (0.2 mm)

**Figure 3.2:** Representation of the transmission rates $T_{ij}$ for input and output particles moving in the most forward direction ($\mu = 0.98$) in aluminium (left) and boron carbide (right). The groups are given by increasing energy and contain neutrons (group 1 to 200) and photons (group 201 to 247). The graphs are divided into four segments, describing the following transitions: $n \rightarrow n$ (top left), $n \rightarrow \gamma$ (top right), $\gamma \rightarrow n$ (bottom left), $\gamma \rightarrow \gamma$ (bottom right).
**Al (10 cm):** Aluminium is used as a spectrum shifter. Most neutrons are transmitted without interactions (along the diagonal) or they lose some of their energy by (in)elastic scattering (below the diagonal). A small amount of the thermal neutrons gains some energy by upscattering. It can be seen that elastic collisions only allow for a limited energy loss for lower-energy neutrons. Fast neutrons can also undergo inelastic collisions resulting in a larger energy loss. Gamma rays are created by thermal neutron capture, but also at resonance peaks for fast neutrons. Many of the incoming photons lose some of their energy by Compton scattering.
**B$_4$C (0.2 mm):** Boron carbide is used as a thermal neutron absorber. This looks almost like a diagonal matrix, which indicates the absence of neutron scattering. A considerable amount of the thermal neutrons is captured by the $^{10}$B nuclei. In 94% of these captures, a 0.48 MeV gamma is emitted, which is clearly visible in the upper right corner. Most incoming photons are transmitted without interactions inside this thin layer.

### 3.3.2 The transport model

The transport matrices $\mathbf{T}$ and $\mathbf{R}$ allow us to calculate the particle flux at any point inside the neutron filter. Suppose the neutron filter consists of $N$ layers. Then, $N+1$ spatial points $x_i$ are positioned between all filter layers ranging from the neutron source at $x_0$ to the beam exit at $x_N$ (see Figure 3.3). The particle flux at spatial point $x_i$ is represented by the two vectors $\vec{\phi}_i^+$ and $\vec{\phi}_i^-$. Here, a distinction is made between particles moving in the positive $x$-direction ($\mu > 0$) and particles moving in the negative $x$-direction ($\mu < 0$). The vector elements of $\vec{\phi}_i^+$ and $\vec{\phi}_i^-$ are the group fluxes $\varphi_{g,m}$ for all 247 energy groups and 8 (either forward or backward) angles at spatial point $i$. Using these definitions, the transmitted and reflected fluxes can be calculated by matrix-vector multiplications. The particle flux $\vec{\phi}_i^+$ is the sum of the transmitted flux $\boldsymbol{T_i}\vec{\phi}_{i-1}^+$ and the reflected flux $\boldsymbol{R_i}\vec{\phi}_i^-$. A similar equality can be formulated for the reverse particle flux. The neutron flux at the entrance of the filter is taken equal to the input spectrum $\vec{\phi}_0^+ = \vec{S}$. At the filter exit, a vacuum boundary condition is applied. This results in the following system of equations:

$$\begin{cases} \vec{\phi}_{i,k}^+ = \boldsymbol{T_i}\vec{\phi}_{i-1,k}^+ + \boldsymbol{R_i}\vec{\phi}_{i,k-1}^- & \qquad \vec{\phi}_0^+ = \vec{S} \\ \vec{\phi}_{i,k}^- = \boldsymbol{T_{i+1}}\vec{\phi}_{i+1,k}^- + \boldsymbol{R_{i+1}}\vec{\phi}_{i,k}^+ & \qquad \vec{\phi}_N^- = \vec{0} \end{cases} \tag{3.6}$$

The particle fluxes are determined by an iterative process. The subscript $k$ indicates the iteration number. In the first iteration, all unknown fluxes are set to $\vec{0}$. Iterations are performed by updating $\vec{\phi}_i^+$ from $i = 1$ to $i = N$, followed by updating $\vec{\phi}_i^-$ from $i = N-1$ back to $i = 0$. This process is repeated until a stationary state is reached. The output spectrum is then given by $\vec{\phi}_N^+$.

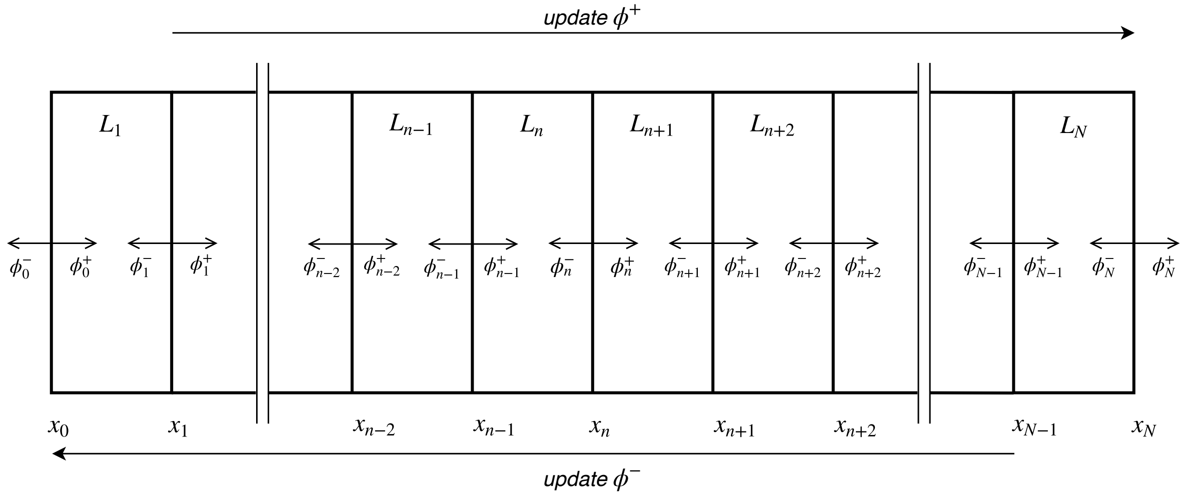

**Figure 3.3:** Schematic overview of the transport model by matrix multiplication. The neutron filter consists of $N$ layers indicated by $L_i$. The particle fluxes $\vec{\phi}_i^+$ and $\vec{\phi}_i^-$ are defined at the boundaries $x_i$ between all layers. Iterations are performed by first updating $\vec{\phi}_i^+$ in the positive $x$ direction and subsequently updating $\vec{\phi}_i^-$ in the reverse direction.

### 3.3.3 Validation with dummy filter

A calculation with a dummy filter has been performed to validate the transport model. The composition of the dummy filter was found in one of the early optimisations. It consists of 25 layers from 6 different materials and has a total length of 76.6 cm. A typical neutron distribution that can be found inside a thermal reactor was used as the input spectrum. The output spectrum was both calculated directly by XSDRN and by the transport model described in the previous section. After 25 iterations, the change in the angular fluxes had become smaller than 0.5% and the calculation was ended. The filtered neutron spectrum matches with the output spectrum from XSDRN as can be seen in Figure 3.4.

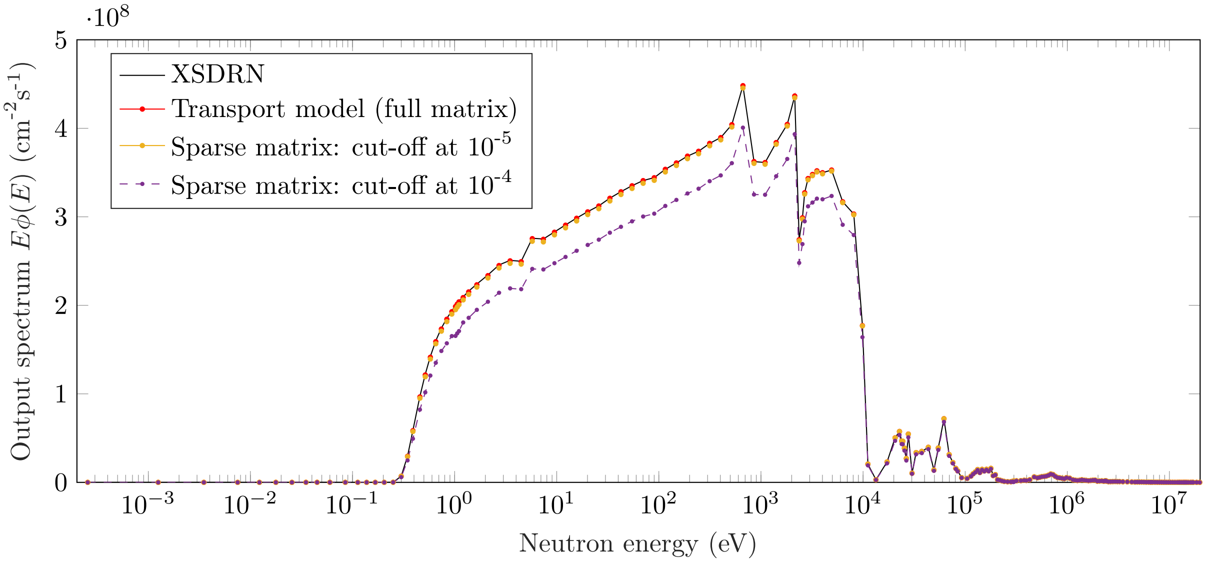

**Figure 3.4:** Validation of the output spectrum by applying the transport model on a dummy filter. The output spectra are shown as $E\phi(E)$ for all neutrons moving at $\mu = 0.98$. After 25 iterations, the output spectrum of the transport model (full matrix) has converged to the output spectrum obtained by XSDRN. The resulting output spectra for two sparse matrix approximations are also given.

Also, the angular dependence of the filtered neutron flux has been compared with a higher-order quadrature calculation in XSDRN (see Figure 3.5). The use of 16 angular directions in the transport model seems to be sufficient for an accurate estimation of the angular distribution. It can be seen that directions with small $\mu$ have weaker intensities in the output spectrum. This can be explained by the longer path lengths these neutrons need to travel within each filter layer, which leads to more absorptions.

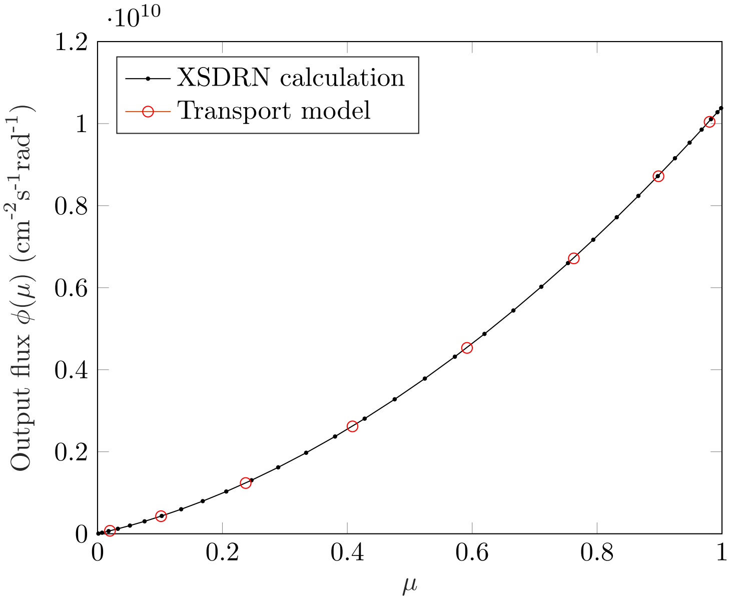

**Figure 3.5:** Validation of the angular distribution $\phi(\mu)$ of the neutrons at the exit of the dummy filter. The flux is summed over all energy groups. The XSDRN calculation is performed with a 64th order double Gauss-Legendre quadrature. The use of 16 angles in the transport model seems sufficient to estimate the angular distribution of the filtered neutron spectrum.

### 3.3.4 Computation time and the use of sparse matrices

The transport model makes it possible to estimate filtered output spectra faster because of the computational effectiveness of matrix multiplications. Fifty calculations similar to the dummy filter calculation have been performed to compare computation times. In each calculation, the composition of the 25 filter layers was determined by a random selection out of 12 materials. In XSDRN, the calculation took 42 seconds of CPU time on average. The computation time has decreased to 3.2 CPU seconds per filter in the simplified transport model if 25 iterations were used. This improvement is of great benefit in the optimisation algorithms, because typically tens of thousands of filter calculations need to done before an optimum is found.

The computation time can be reduced further by the use of sparse matrices. Many of the transmission and reflection matrices are relatively empty with lots of zeros on off-diagonal elements (see for example the elements $T_{ij}$ for boron carbide in Figure 3.2). In this case, it could be beneficial to switch from full to sparse matrices. This means only nonzero elements of the matrix are stored together with their indices. Also, operations on zero elements are eliminated, which can reduce computation time. Before the transport matrices are converted to sparse matrices, a cut-off value needs to be chosen. All values $T_{ij}$ and $R_{ij}$ below this cut-off value are set to zero. Different cut-off values have been tested in the random filter calculations. There is a slight improvement in computation time for a cut-off value of $10^{-5}$ or higher. At the same time, the estimated output spectrum becomes less accurate because a fraction of the matrix elements has been neglected. Figure 3.6 shows how the error in the output spectrum develops for different cut-off values. Here, a trade-off can be made between calculation speed and accuracy of the estimated spectrum, by choosing the number of iterations and the cut-off value. In the remainder of this thesis, it was decided to perform all filter calculations using sparse matrices with a cut-off at $10^{-5}$ and 25 iterations.

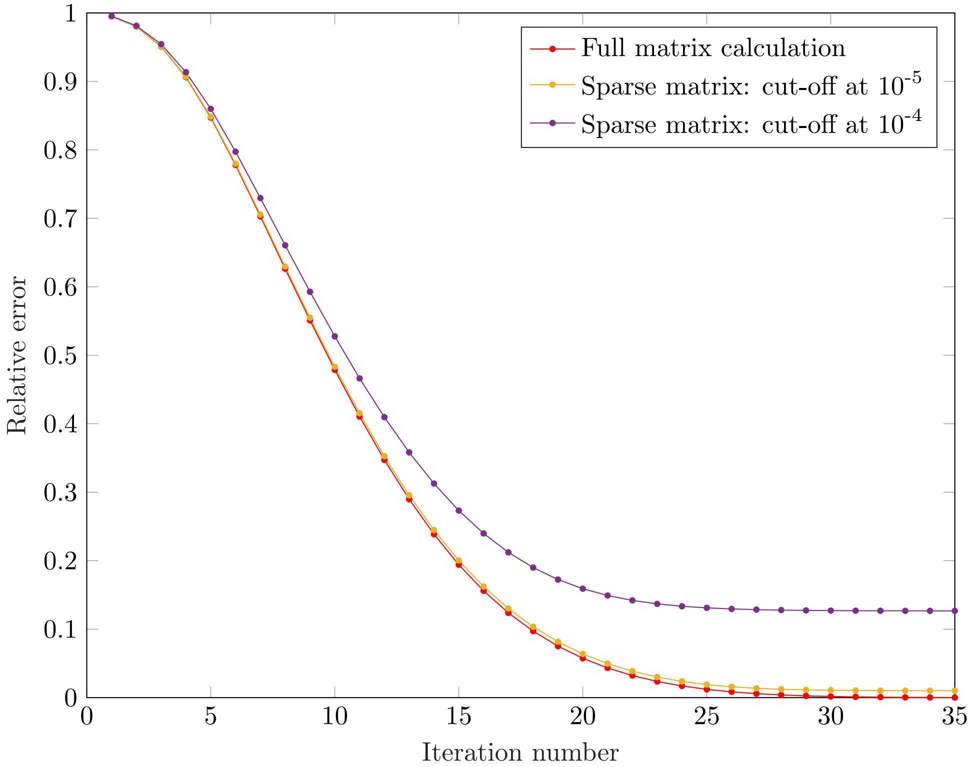

**Figure 3.6:** Comparison of the relative error in the output spectrum as a function of the iteration number for full and sparse matrix calculations. The transport model was used for one of the randomly generated neutron filters which consists of 25 layers. The relative error is defined as $\frac{||\phi_g-\hat{\phi_g}||}{||\phi_g||}$, where the norm is taken of the difference between the estimated group fluxes $\hat{\phi_g}$ and the in XSDRN calculated group fluxes $\phi_g$. The average computation time is 1.2 s for a cut-off at $10^{-4}$ and 2.0 s for a cut-off at $10^{-5}$ using 25 iterations. There is no significant improvement in computation time for a cut-off at $10^{-6}$ compared to the full matrix approach. The computation times are approximately proportional to the number of iterations.

# 4 | Dose Calculation

After filtering, the neutron beams continue their ways inside the patient towards the tumour. The neutrons inside the body induce various nuclear reactions in which ionizing radiation is released. These energetic particles can deliver a dose to the tumour, but also healthy tissue can be damaged by unwanted radiation. In this chapter it is described how the particle fluxes are estimated inside the patient and how the resulting dose distributions are derived from there.

## 4.1 Monte Carlo particle transport inside the patient

The Monte Carlo method is a statistical approach to find the solution of the Boltzmann transport equation. In this method, the trajectories of individual particles are tracked from their source until their disappearance. Along their trajectories, particles undergo a series of events which are determined by their interaction probabilities. These events can change the direction and energy of the particles, produce secondary particles or lead to the end of a particle track. By repeated sampling of source particles and possible interactions, estimations of the particle fluxes and reaction rates inside the patient can be obtained. In this thesis, the Monte Carlo N-Particle (MCNP) code by Los Alamos National Laboratory [36] was used.

The Monte Carlo code needs a description of the geometry and material composition of the tissues to calculate the interaction probabilities of the neutrons and photons. In realistic treatment planning, one would normally determine the tissue composition of the patient by using MRI or CT data. These images have a resolution of typically 1-2 mm and ideally this data should be implemented in the Monte Carlo code. Unfortunately, MCNP is not optimised for using such a detailed geometry description [35]. The code works more efficient and faster when particle tracks are simulated through less complicated geometries. Therefore, only simplified phantoms are used in this thesis. They consist of simple geometric volumes in which material concentrations are taken constant.

The trajectories of particles are tracked within finite volumes inside the phantom. These finite volumes are defined by applying a three-dimensional grid over the entire volume. The cubes that are created this way are called voxels. The voxel size determines at which level spatial information can be estimated. Smaller voxels provide a higher spatial resolution, but this also leads to higher variance and longer convergence times in the simulations. In practice, the voxel size is often limited by the resolution of MRI or CT images.

In MCNP, various quantities can be estimated on a voxel level by applying a track-length tally (FMESH4). The scalar particle flux for example, can be approximated inside each voxel by an estimator based on the track lengths $L_{track}$ of these particles inside the voxel volume $V$. The estimator for this flux (normalized per source particle) is given by

$$\hat{\varphi} = \frac{1}{N} \sum_{tracks} \frac{L_{track}}{V}, \tag{4.1}$$

where $N$ is the total number of simulated source particles. Similarly, these track-length tallies can be used to estimate reaction rates and dose values in each voxel.

## 4.2 Dose estimations inside test phantom

### 4.2.1 Four major dose components in BNCT

Absorbed dose is defined as deposited energy per unit mass and can be measured in gray (1 Gy = 1 J/kg). The energy deposition is caused by ionizing particles which are created in nuclear reactions. There is a large variety of possible reactions of neutrons with nuclei in human tissue, mainly with $^{1}$H, $^{12}$C, $^{14}$N, $^{16}$O and of course the injected $^{10}$B. In practice, the total absorbed dose in BNCT can be reduced to the contributions of four major dose components. These dose components are:

- The **boron dose**, which is caused by the previously described neutron capture reaction in $^{10}$B. This reaction is the reason to apply BNCT and this dose component inside the tumour needs to be large compared to the other dose components for the treatment to be effective.
- The **nitrogen dose** is caused by thermal neutron capture in $^{14}$N. In this reaction, a 620 keV short range proton is emitted. Although nitrogen has a lower neutron capture cross section than boron, its concentration in tissue is much higher. These capture reactions outside the tumour result in unwanted tissue damage; it comprises 96% of the energy deposition in healthy tissue due to thermal neutrons [37]. Also, it reduces the total number of thermal neutrons that can reach the tumour.
- The **fast neutron dose** is caused by high-energy neutrons scattering with $^{1}$H. In this collision, the proton can be knocked out of the hydrogen atom, leaving with half the energy of the incoming neutron on average. Having an energy of a few MeV at most, also these protons have relatively short ranges in tissue. This single reaction is responsible for about 90% of the total energy deposition in healthy tissue due to neutrons between 600 eV and 3 MeV [37]. It mostly affects the skin because neutrons have the highest energy directly after entering the body.
- The **gamma dose** comes from different sources. Photons can already be present inside the neutron beam or they can be created in capture reactions. The largest contribution comes from the 2.22 MeV photon that is emitted after thermal neutron capture in $^{1}$H. Also in the boron capture reaction a gamma ray is emitted in 94% of all cases. This gamma has less impact with an energy of 0.48 MeV.

Some of the characteristics of these dose components are summarized in Table 4.1. In the first three dose components, the track lengths of the ionizing particles are much smaller than the typical voxel size. Therefore, it is assumed that all energy is deposited locally. In case of the gamma dose $D_\gamma$, the energy is deposited differently. Gamma rays are indirectly ionizing because they deposit their energy by secondary electrons which are created in the photoelectric effect, Compton scattering or pair production. A kerma approximation is used to estimate the absorbed photon dose. Kerma is defined as the kinetic energy released per unit mass and consists of the energy that is transferred after the first collision [38]. At low gamma energies, kerma approximately equals the absorbed dose, since most of the initial kinetic energy of the electrons is deposited within the same region. In case of a charged particle equilibrium, kerma and absorbed dose are equal. The approximation becomes less accurate at higher energies, because some highly energetic secondary electrons or X-rays can escape the region of interest before depositing their energy. In that situation, the absorbed dose would be overestimated by the kerma approximation.

**Table 4.1:** Overview of the four major dose components in BNCT.

| **Symbol** | **Name** | **Reaction** | **Released energy** |
|---|---|---|---|
| $D_B$ | Boron dose | $^{10}$B(n,$\alpha$)$^{7}$Li | 2.34 MeV $^{*}$ |
| $D_N$ | Nitrogen dose | $^{14}$N(n,p)$^{14}$C | 620 keV |
| $D_H$ | Fast neutron dose | $^{1}$H(n,n)p | Half the neutron energy on average |
| $D_\gamma$ | Gamma dose | $^{1}$H(n,$\gamma$)$^{2}$H $^{**}$ | 2.22 MeV |

$^{*}$) Gamma energy not included

$^{**}$) The largest contribution of many possible reactions

### 4.2.2 Calculation of the dose components in MCNP

In MCNP, it is possible to convert track-length based flux estimators (given in Equation 4.1) to dose tallies. The estimated absorbed dose in a voxel then becomes

$$\hat{d} = \frac{1}{N} \sum_{tracks} \frac{L_{track}}{V} \rho_a \sigma(E_{track}) H(E_{track}). \tag{4.2}$$

For each dose component, the estimated flux is multiplied by the microscopic cross section of the reaction of interest $\sigma(E)$, the released energy or heating number $H(E)$ and the atomic density $\rho_a$ of the nuclide that is involved in this reaction. MCNP uses internal libraries which contain values for the cross sections and heating numbers. For the gamma dose, a similar expression is used containing flux-to-kerma conversion factors. In MCNP, dose values $\hat{d}$ are given in units of MeV/cm$^3$ per source particle. Using the mass density of the tissue, these values are converted to arrive at the absorbed dose in Gy per source particle.

The absorbed dose values have been calculated inside a test phantom to investigate the effects of the various dose components. The test phantom consists of an ellipsoid with outer dimensions of 20.6 cm, 17.6 cm and 14.6 cm. A spherical tumour of 3 cm in diameter is positioned at the centre of the ellipsoid. ICRU four-component soft tissue was used for the atomic composition inside the entire phantom [20]. Boron-10 was added inside the tumour (35 ppm) and inside the healthy tissue (10 ppm). A mono-directional disk source with a diameter of 3 cm was placed along the shortest axis of the ellipsoid directly pointing towards the tumour. The voxel size was taken 2 mm in each dimension. The four dose components have been calculated for 247 different beamlets. The energies of these beamlets correspond to the mean energies of the 200 neutron groups and 47 gamma groups that were also used in the XSDRN calculation. For each beamlet, $10^7$ source particles were used. The computation times of these simulations were about 30 minutes per beamlet in MCNP running on 3 cores. Figure 4.1 shows the dose components that were found inside the test phantom for three different neutron energies.

From the $D_B$ components, it can be seen that the $^{10}$B(n,$\alpha$)$^7$Li reactions occur at different locations depending on the incident neutron energy. Thermal neutrons are captured directly after entering the tissue. The 1 keV neutrons penetrate deeper into the tissue, which results in neutron captures both inside the healthy tissue and inside the tumour. The fast neutron beam of 1 MeV produces most of the capture reactions inside the tumour, which seems highly beneficial. At this energy however, the fast neutron dose causes severe damage to the healthy tissue. The absorbed dose values of the $D_H$ component are about two orders of magnitude larger than the $D_B$ component at 1 MeV. For the two lower energetic neutron beams, the $D_H$ component has minimal influence on the total dose distribution. Both the $D_N$ and $D_\gamma$ component are delivered non-selectively affecting both the tumour and healthy tissue. Neutrons of higher energies suffer a larger number of scattering interactions before they are absorbed. This results in a wider spread of these dose components inside the phantom for fast neutrons compared to thermal neutrons.

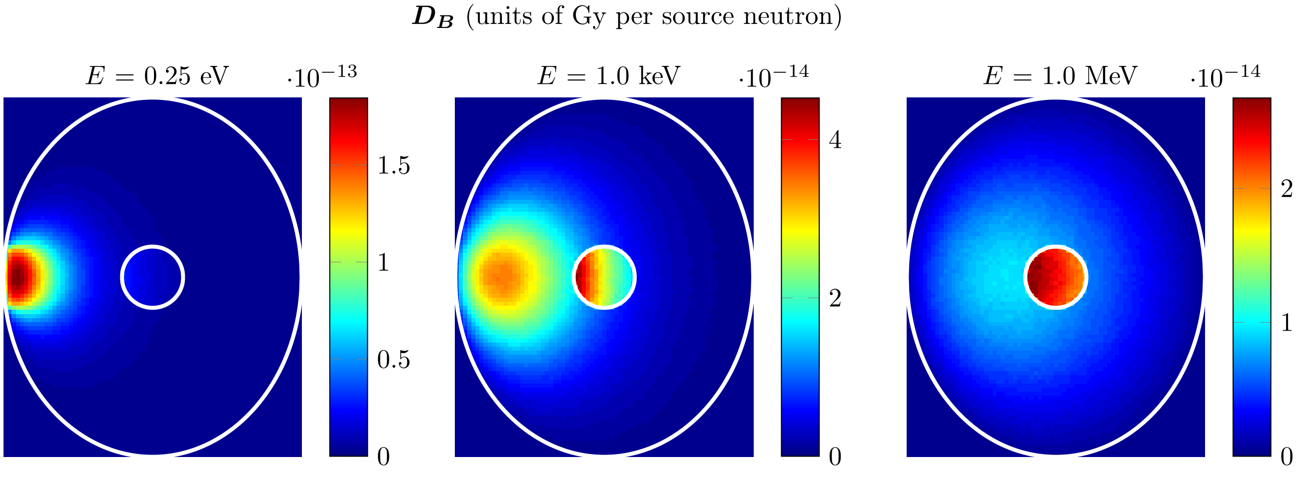
$\boldsymbol{D_B}$ (units of Gy per source neutron)

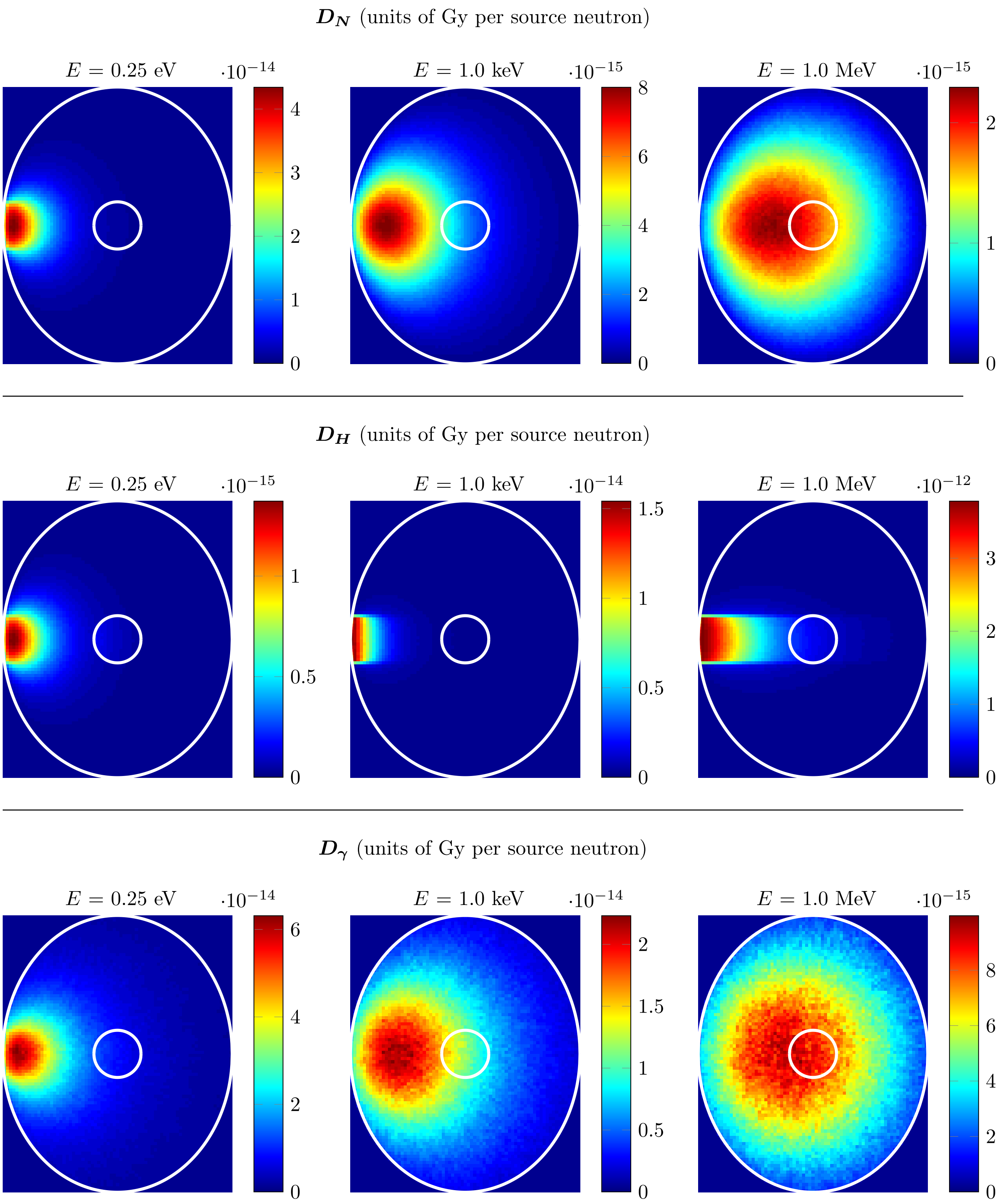

**Figure 4.1:** Dose distributions of the four dose components inside the test phantom delivered by neutrons of 0.25 eV, 1 keV and 1 MeV. The mono-directional disk source (diameter = 3 cm) is positioned at the left side of the phantom. The neutrons are emitted in the direction normal to the ellipsoid boundary.

### 4.2.3 Biologically weighted dose

Each type of ionizing radiation deposits its energy differently in tissue. A higher density of ionizations along particle tracks results in a stronger biological effect in comparison with the same physical dose of low LET radiation. For this reason, weights are used to compare different dose components. These weights are called relative biological effectiveness (RBE) factors. The RBE factor of the gamma dose is taken equal to one and the other factors have been determined experimentally with respect to this reference value. This way, a biologically weighted dose is defined in terms of gamma dose equivalents which is usually expressed in Gray-Equivalent (Gy-Eq). In further chapters, the biologically weighted dose will simply be referred to as dose, denoted by $D$.

The biological effects caused by the boron dose depend not only on the type of radiation, but also on the specific boron compound that is used. Therefore, $D_B$ is weighted with a compound biological effectiveness (CBE) factor instead. The CBE factor depends on many different parameters, such as the mode of drug administration, the boron distribution within the cells and the size of the nucleus within the target cell population [1]. As a result, the CBE factor can be different in each tissue. For efficient boron compounds, the CBE factor is higher inside the tumour than in healthy tissues.

After many years of research, the values of these factors are still under discussion [38]. In this thesis, RBE and CBE factors are taken from currently available experimental data [39, 40]. The resulting biologically weighted dose distributions inside the test phantom are shown in Figure 4.2 for some of the beamlets. The healthy cells receive most of the unwanted dose from the $D_N$ component for lower-energy neutron beams and from the $D_H$ component for higher-energy neutron beams. Also, it can be seen that a single neutron beam is not capable of effectively irradiating the back side of the tumour in this configuration. Additional neutron beams from different angles are needed to obtain a better dose distribution.

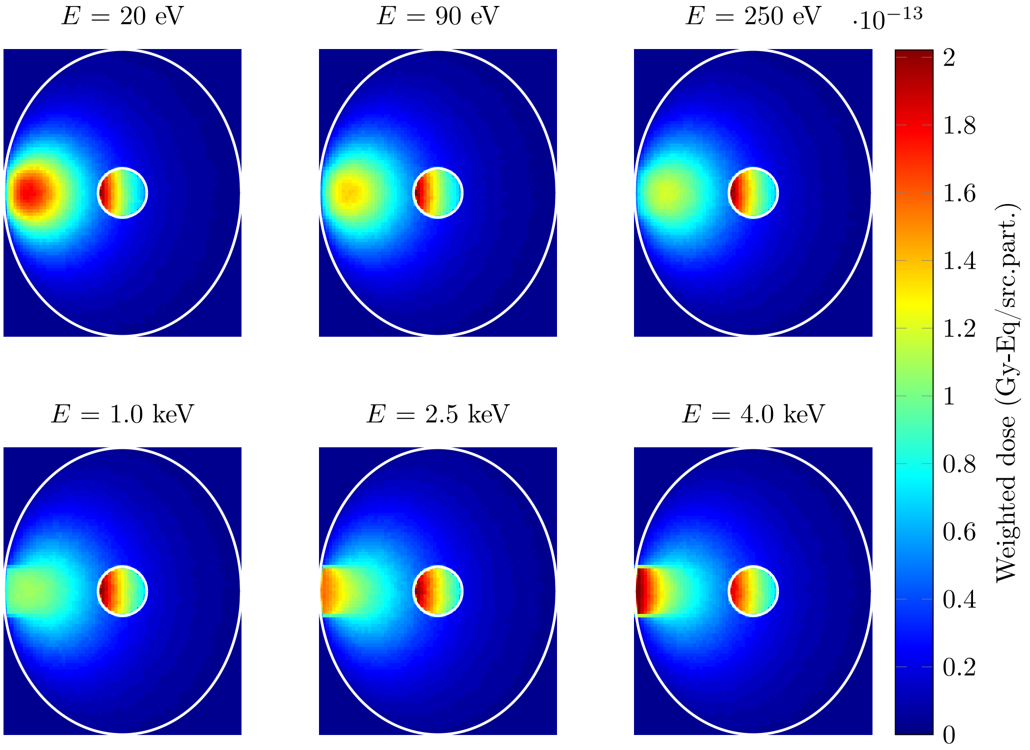

**Figure 4.2:** Biologically weighted dose distributions in the test phantom for six different epithermal neutron beams. The weighted dose is defined as the sum of the four dose components using the RBE and CBE factors as weights. The following values are used: $\mathrm{RBE}_\gamma = 1$, $\mathrm{RBE}_\mathrm{N} = \mathrm{RBE}_\mathrm{H} = 3.2$, $\mathrm{CBE}_\mathrm{B} = 3.8$ inside the tumour and $\mathrm{CBE}_\mathrm{B} = 1.3$ in healthy tissue.

# 5 | The Model Problem

## 5.1 Problem description

In this chapter, a model problem is formulated which serves as a tool to test the optimisation algorithms that are discussed in Chapter 6 en 7. The problem describes a simplified case of a patient with a brain tumour that is treated with BNCT. The aim is to find the optimum neutron filter design for this specific case.

### 5.1.1 Phantom geometry

The patient's brain is represented by a modified version of the Snyder head phantom [41] (see Figure 5.1). The boundaries of the tissues are defined by three ellipsoids given by the following surfaces:

$$\left(\frac{x}{8.8}\right)^2+\left(\frac{y}{10.3}\right)^2+\left(\frac{z}{7.3}\right)^2=1, \qquad \left(\frac{x}{8.3}\right)^2+\left(\frac{y}{9.8}\right)^2+\left(\frac{z}{6.8}\right)^2=1, \qquad \left(\frac{x}{7.5}\right)^2+\left(\frac{y}{9}\right)^2+\left(\frac{z}{6}\right)^2=1.$$

Here, the dimensions are given in centimeters. The inner ellipsoid encloses the brain tissue and is surrounded by an 8 mm thick skull and a 5 mm thick scalp. The dimensions of the outer ellipsoid are 17.6 cm, 20.6 cm and 14.6 cm in the $x$-, $y$- and $z$-direction. The tumour region is defined by a sphere with a radius of 2 cm with its centre at $(x, y, z) = (-\frac{3.5}{\sqrt{2}}, -\frac{3.5}{\sqrt{2}}, -2)$ at the lower part of the brain touching the brainstem. The brainstem is modelled as a cylinder with a diameter of 3 cm centered around the $z$-axis between $z = -6$ and $z = 0$. Within each tissue, the composition is assumed to be homogeneous with densities and atomic fractions taken from Lawrence Berkeley National Laboratory [42]. All tissues contain $^{1}$H, $^{12}$C, $^{14}$N and $^{16}$O. Inside the skull, $^{31}$P and $^{40}$Ca are added as well (see Table 5.1). BPA is used as boron compound, which is modelled by adding 10 ppm of $^{10}$B in the healthy tissues and 35 ppm in the tumour.

**Table 5.1:** Atomic composition of the tissues given in mass percentages.

| | $\rho$ (g/cm$^3$) | $^{1}$H | $^{12}$C | $^{14}$N | $^{16}$O | $^{31}$P | $^{40}$Ca |
|---|---|---|---|---|---|---|---|
| **Skin** | 1.07 | 10.4 | 23.7 | 2.7 | 63.0 | 0.0 | 0.0 |
| **Bone** | 1.61 | 5.0 | 21.1 | 4.0 | 43.4 | 8.1 | 17.6 |
| **Brain** | 1.05 | 10.6 | 14.0 | 1.8 | 72.6 | 0.0 | 0.0 |

### 5.1.2 Organs at risk

In each treatment, organs at risk (OAR) need to be identified and protected from receiving too much dose. Some of the possible organs at risk in the brain are the optic chiasm, brainstem, hippocampus, retina and eye lenses [43]. In this model problem, only the brainstem is taken into account because of the tumour location. The brainstem connects the brain to the spinal cord and maintains vital control of the heart and lungs. If the absorbed dose inside the brainstem becomes too high, symptomatic necrosis can occur, which leads to a decrease in cognitive functioning. A maximum dose constraint of 45 Gy-Eq is used in the brainstem [44]. In the phantom description, OARs are assumed to have the same composition as their surroundings. For this reason, the locations of OARs do not influence the resulting dose distribution. This makes it possible to add more OARs after the dose calculations have been performed if one wishes to extend the model problem.

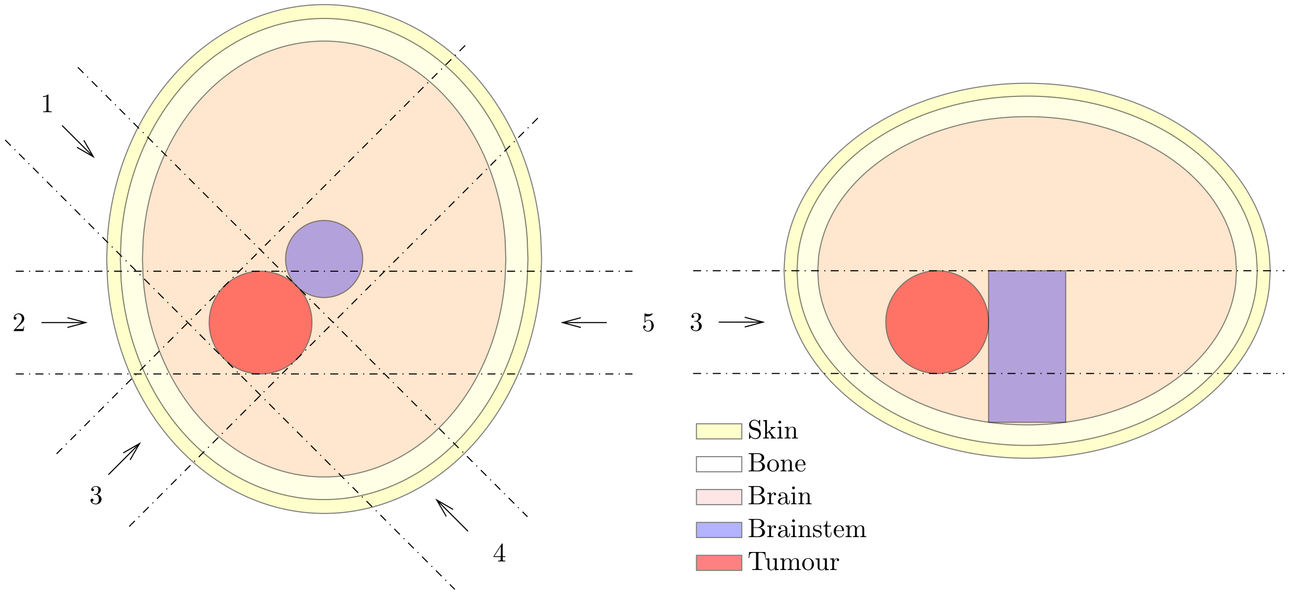

**Figure 5.1:** Intersections of the problem geometry. The left image shows the intersection in the $xy$-plane at $z = -2$. The right image shows the intersection in the vertical plane along beam direction 3. All regions are defined by simple geometric volumes. The atomic compositions are constant within each region. The tumour is irradiated by five neutron beams which are denoted by the arrows between the dashed lines.

### 5.1.3 Beam directions

Five possible beam directions are chosen to irradiate the patient. In practice, this can be achieved by rotating the patient around a fixed neutron beam and changing the neutron filter for each direction. The beam diameter is chosen equal to the tumour diameter. The directions are selected in such a way that their paths towards the tumour are short or without intersection of the OAR. Also, it is important to irradiate the tumour from multiple different sides to obtain a uniform dose distribution within the tumour. A single neutron beam is not always able to deliver a sufficient amount of dose to the backside of a deep tumour as was shown in Figure 4.2. The optimisation algorithm has the freedom to neglect one or more of these beam directions if this leads to better results.

### 5.1.4 Objective function

The optimisation is performed by minimising the cost function $F$, which is defined as

$$F = \sum_i w_i (D_i - P_i)^2. \tag{5.1}$$

Here, $P_i$ is the prescribed dose in voxel $i$ and $D_i$ is the actual dose in voxel $i$. The squared differences are summed over all voxels using weights $w_i$, which can be used to increase the importance of specific voxels. In fact, the weights and prescribed dose values are defined for regions (denoted by subscript $r$). These regions include the various tissues and the tumour. A dose of $P_r = 60$ Gy-Eq is prescribed to the tumour. In all other regions, $P_r$ is taken equal to zero. Some of the voxels which are located at the boundaries between regions, are occupied by more than one region. In these voxels, $P_i$ and $w_i$ are determined by taking an average over the various regions of interest. For example, the weight of a voxel which comprises multiple regions becomes $w_i = \sum_r f_{i,r} w_r$, where $f_{i,r}$ is the fraction of voxel $i$ that is occupied by region $r$. Similarly, the prescribed dose in a voxel is $P_i = \sum_r f_{i,r} P_r$.

### 5.1.5 Description of the neutron source

As in the majority of the performed BNCT trials, we assume a thermal research reactor is used as neutron source. To yield a high beam intensity, the idea is to build the neutron filter inside one of the beam tubes, similar to the neutron filter at the HFR in Petten [45]. The neutron spectrum at the entrance of the beam tube is approximated by:

- a Maxwell-Boltzmann distribution with maximum intensity at 25 meV in the thermal energy range,
- a $1/E$ dependence in the epithermal energy range,
- the Watt fission spectrum of $^{235}$U in the fast energy range.

As a reference frame, some information about the neutron spectrum at the HOR was used. At the entrance of beam tube L1, the total neutron flux is about $10^{11}$ cm$^{-2}$s$^{-1}$ and the spectrum consists of 60% thermal neutrons, 14% epithermal neutrons and 26% fast neutrons. In our input spectrum, the same relative intensities were applied. It was decided to use a higher source strength to make it more likely that the prescribed dose could be delivered within a reasonable treatment time. The HOR in Delft is operated at a thermal power level of 2 MW [46]. One of the most powerful research reactors is the 100 MW BR2 reactor in Belgium [47]. This reactor type is assumed to be available as neutron source in the model problem. Given that the total neutron flux is approximately proportional to the reactor power, this would correspond to a scalar flux of $5 \cdot 10^{12}$ neutrons cm$^{-2}$s$^{-1}$ at the beam tube entrance. The resulting energy spectrum is shown in Figure 5.2.

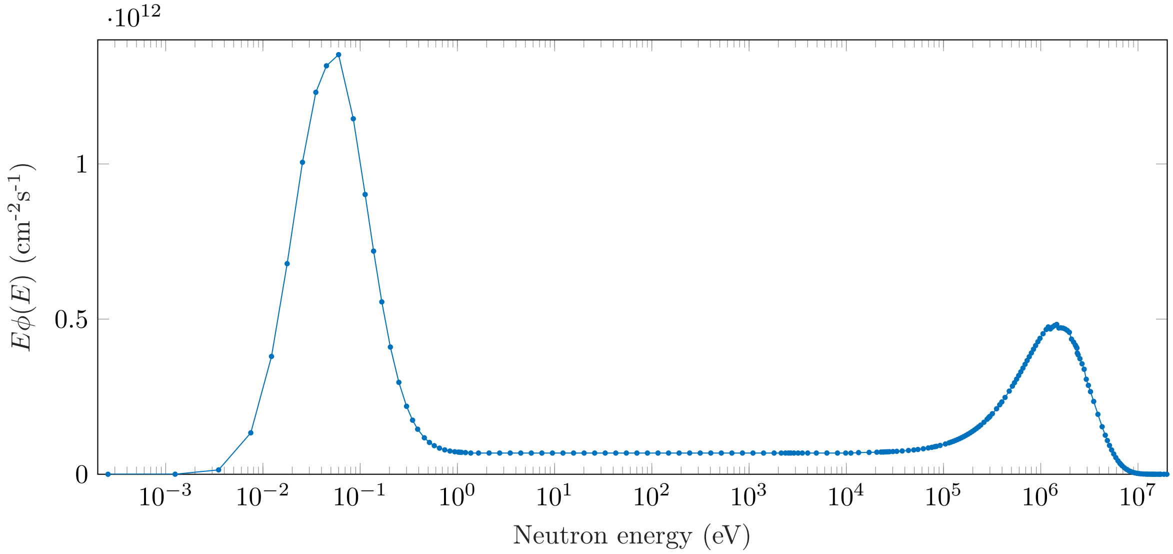

**Figure 5.2:** Energy spectrum of the neutron source given as $E\phi(E)$ for 200 neutron energies corresponding to the energy groups used in XSDRN. The spectrum represents the neutron flux at the beam tube entrance of a high-power research reactor approximated by theoretical distributions in the thermal, epithermal and fast energy range with relative intensities of 0.60, 0.14 and 0.26 respectively. The energy integrated neutron flux is $5 \cdot 10^{12}$ neutrons cm$^{-2}$s$^{-1}$.

For simplicity, the flux at the entrance of the beam tube is assumed to be isotropic[1]. The group fluxes $\varphi_{g,m}$ are determined by integrating the energy-dependent flux $\phi(E)$ over the energy groups and multiplying by the Gauss-Legendre quadrature weights $w_m$,

$$\varphi_{g,m} = w_m \int_{E_g} \phi(E) dE. \tag{5.2}$$

---

[1] In fact, an angular dependence of $\varphi(\theta) \sim \sin\theta$ was applied in the optimisations. This distribution was considered unrealistic and therefore all results have been recalculated for an isotropic source flux. This resulted in equal relative dose distributions and a somewhat shorter treatment time.

The quadrature weights are defined in such a way that $\sum_m w_m = 1$. This means that the summation over all group fluxes is equal to the total flux of $5 \cdot 10^{12}$ neutrons cm$^{-2}$s$^{-1}$. Half of these neutrons is moving in the positive $x$-direction ($\mu > 0$). In the transport model, these group fluxes are inserted in the vector $\vec{\phi}_0^+$ as explained in Section 3.3.2. A fraction of 2.5% of all source neutrons enters the neutron filter in the most forward direction of $\mu = 0.98$.

Finally, the gammas were added to the source spectrum. No spectrum was available at the same location as the neutron source. Instead, a gamma spectrum was taken at the exit of beam tube L1 and scaled to estimate the actual intensity (see Figure 5.3). The gamma group fluxes were determined similarly as was described for the neutron group fluxes.

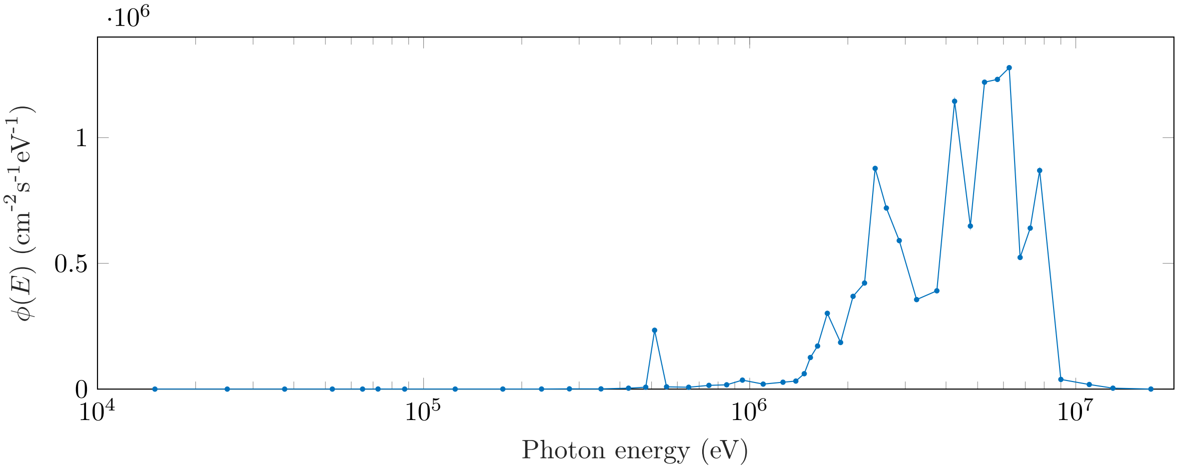

**Figure 5.3:** Energy spectrum of the gammas in the beam given as $\phi(E)$ for 47 photon energies corresponding to the energy groups used in XSDRN. The spectrum is an amplified version of the spectrum taken at the exit of beam tube L1 at the HOR.

## 5.2 Calculation scheme

For a given set of filter compositions, the objective function is evaluated by the following calculation scheme. For each neutron beam $b$, the procedure consists of two steps: a filter calculation, followed by a dose calculation.

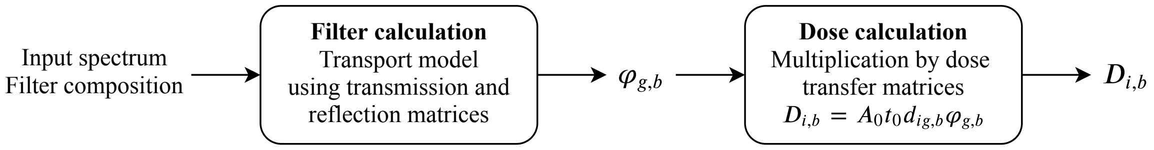

For a given input spectrum and filter composition, the resulting output spectrum is determined by the iterative process as described in Chapter 3. The transmission and reflection matrices which are needed here, have been calculated before the optimisation starts. The filtered spectrum is given by $\varphi_{g,m,b}$, which contains the group fluxes (units of cm$^{-2}$s$^{-1}$) in energy group $g$ and angular direction $m$ in beam $b$. This neutron beam is collimated and it is assumed that only the particles moving in the most forward direction $\mu_m = 0.98$ are transmitted. These group fluxes $\varphi_{g,b}$ are selected and used as input in the dose calculation.

The dose calculation is performed by multiplying the group fluxes by $A_0$, $t_0$ and $d_{ig,b}$. This product contains the beam area $A_0 = 12.6$ cm$^2$ and a standard treatment time of $t_0 = 3600$ s. The treatment time is adjusted at a later stage in the algorithm. The dose transfer matrix contains the elements $d_{ig,b}$, which are equal to the delivered dose in voxel $i$ if a particle of energy group $g$ enters the phantom from beam direction $b$. For simplicity, all collimated beams are assumed to enter the tissue at normal incidence ($\mu = 1$). The dose transfer matrices have been calculated beforehand in MCNP as described in Chapter 4.

When the dose contributions from the different beams $D_{i,b}$ are known, the next step is to determine how long the patient should be irradiated from each beam direction. A relative treatment time $t_b$ is assigned to each beam. The total dose distribution then becomes $D_i = \sum_b t_b D_{i,b}$, which should resemble the prescribed dose $P_i$ as much as possible. To achieve this, the relative treatment times are determined by the method of least squares. It is convenient to express this in matrix form. The prescribed dose is represented by a column vector $\vec{P}$, the dose contributions $D_{i,b}$ are grouped together as columns in $\boldsymbol{D}$ and the voxel weights $w_i$ from Equation 5.1 are placed on the diagonal of $\boldsymbol{W}$:

$$\vec{P} = \begin{bmatrix} P_1 \\ \vdots \\ P_N \end{bmatrix}, \qquad \boldsymbol{D} = \begin{bmatrix} \vdots & & \vdots \\ D_{i,1} & \dots & D_{i,5} \\ \vdots & & \vdots \end{bmatrix}, \qquad \boldsymbol{W} = \mathrm{diag}(w_1, ..., w_N)$$

The weighted least squares solution of the relative treatment times $t_b$ then becomes

$$\vec{t} = (\boldsymbol{D}^T \boldsymbol{W} \boldsymbol{D})^{-1} \boldsymbol{D}^T \boldsymbol{W} \vec{P}. \tag{5.3}$$

The final dose distribution $D_i$ is then determined and inserted in Equation 5.1 to arrive at the cost value $F$.

## 5.3 Preliminary optimisations

Before the filter compositions are optimised, some preliminary optimisations have been performed. Here, the goal was to find the optimum energy spectra of the neutron beams. This was done by omitting the filter calculation and taking the group fluxes $\varphi_{g,b}$ as input variables of the optimisation. The neutron and gamma beamlets are defined for 247 energy groups and 5 beam directions. The optimisation of these 1235 parameters was performed by the interior-point algorithm using the *fmincon* function in Matlab. The cost function (Equation 5.1) was used as the objective function and the gradient was included as well. Equal values of $\varphi_{g,b} = 10^7$ cm$^{-2}$s$^{-1}$ were used for all $g$ and $b$ as the starting point and a lower bound of zeros was applied. The algorithm was terminated when the first-order optimality had become smaller than $10^{-3}$. No more than 65 function evaluations were needed to arrive at this point.

The optimisations have been performed for different combinations of tissue weights. These four cases are specified in Table 5.2. The resulting optimum dose distributions that were found for these cases are shown in Figure 5.4 and the corresponding dose volume histograms are given in Figure 5.5. It can be seen that the maximum dose in the brainstem remains below the imposed dose constraint. This dose can be reduced further by increasing the OAR weight. Similarly, a higher and more uniform tumour dose can be obtained by increasing the tumour weight. For all cases however, the dose distribution inside the tumour shows a relatively wide spread. It is expected that this dose uniformity can be improved somewhat by increasing the tumour weight further at the cost of a higher dose in the OAR.

A standard treatment time of 1 hour was applied for each beam. In case C and D, this has led to average beam intensities of $\sim 2 \cdot 10^9$ neutrons cm$^{-2}$s$^{-1}$ that were needed to perform the treatment. Using the neutron source that is described in Section 5.1.5, these beam intensities can be achieved if about two percent of the source neutrons in the most forward angular direction are transmitted through the neutron filters.

**Table 5.2:** Tissue weights that have been applied in the four optimisations.

| **Region** | **A** | **B** | **C** | **D** |
|---|---|---|---|---|
| Tumour | 1 | 10 | 30 | 30 |
| OAR | 1 | 1 | 1 | 10 |
| Other | 1 | 1 | 1 | 1 |

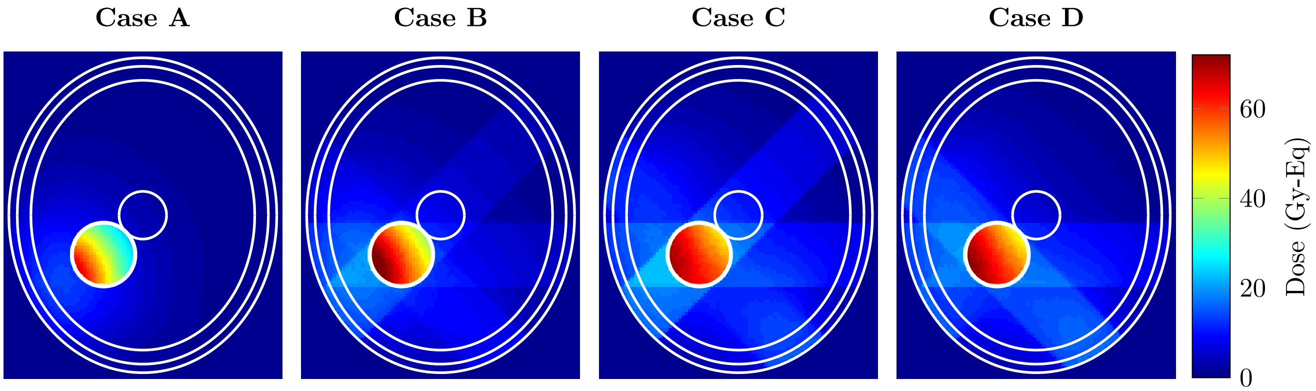

**Figure 5.4:** Optimum dose distributions found by optimising the particle fluxes $\varphi_{g,b}$ with the interior-point algorithm. The voxel weights in the tumour and OAR are varied as is shown in Table 5.2.

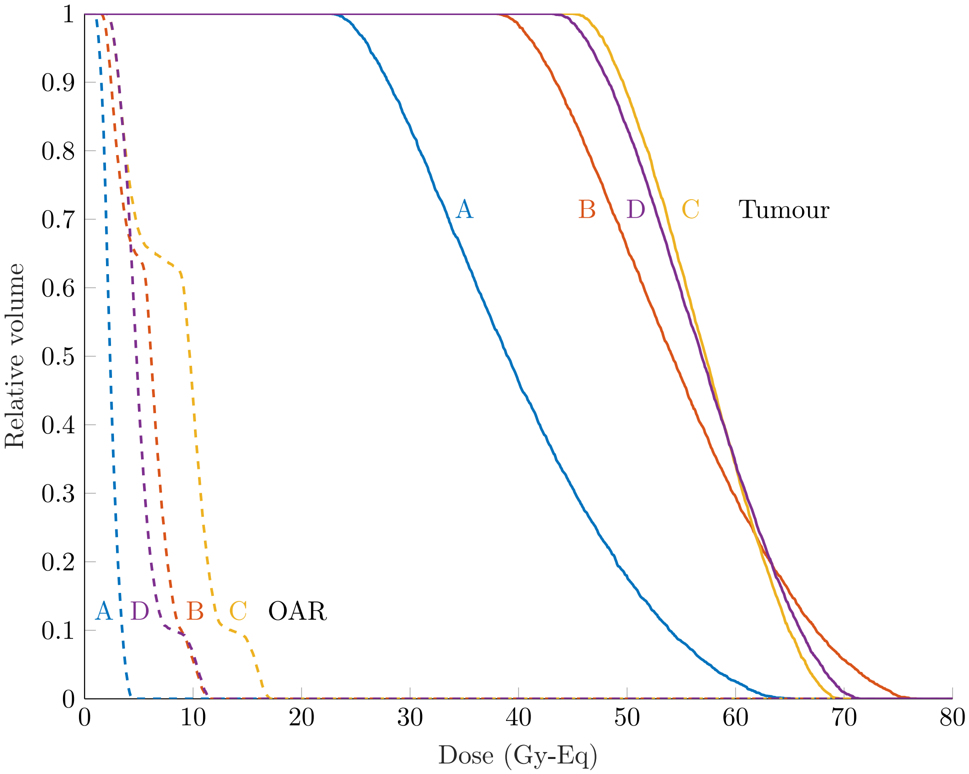

**Figure 5.5:** Dose volume histograms in the tumour and organ at risk for the different cases.

Finally, the optimised group fluxes have been analysed. The gamma fluxes were found to be zero everywhere. The neutron spectra are characterized by sharp peaks between 1 and 4 keV. The relative neutron beam intensities vary strongly depending on the chosen weights. In most of the beam directions, only a few neutron energies are present (see Figure 5.6). It can be seen that a finer group structure is required to describe the optimum neutron spectra more accurately. In order to do this, additional dose transfer matrices are needed for a number of intermediate neutron energies. In practice, it will be difficult to develop a neutron filter that is able to generate such a narrow output spectrum, since the input spectrum comprises a wide range of energies. Therefore, it is still useful to apply the broader group structure in the filter optimisations. In the following chapters, voxel weights from case D are applied in all optimisations.

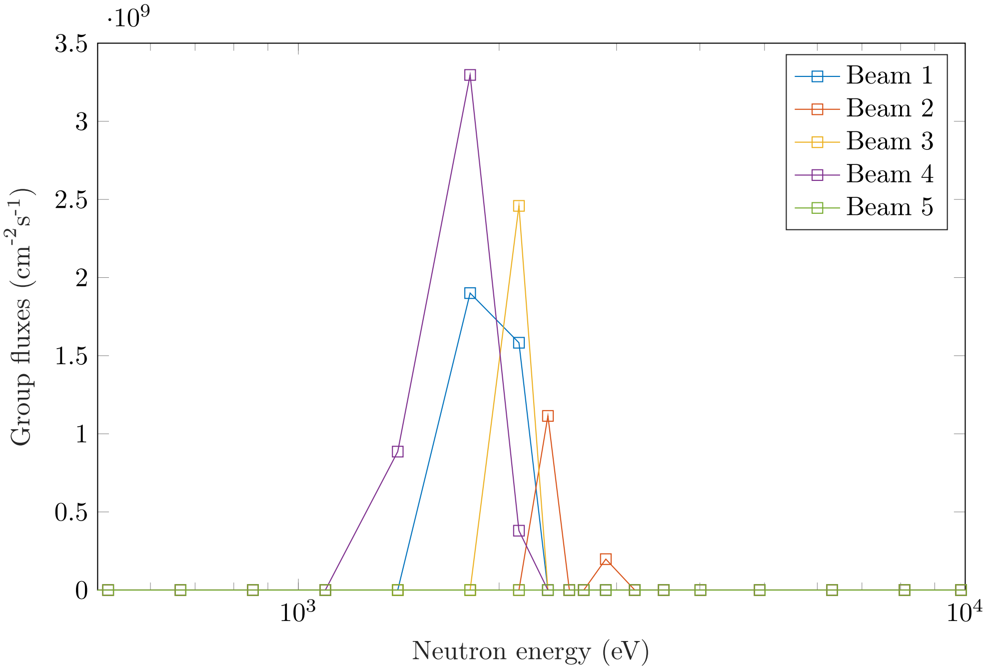

**Figure 5.6:** Optimised group fluxes for each neutron energy and beam direction corresponding to case C.

# 6 | Filter Optimisation by a Gradient Descent Algorithm

A large class of optimisation algorithms is based on the principle of gradient descent. In these algorithms, the strategy is to evaluate the function value repeatedly at different points by taking steps proportional to the negative of the gradient. This way, a minimum of the objective function can be found. If we want to apply this on filter optimisation, the problem needs to be formulated in such a way that the objective function is differentiable with respect to the input variables. Because of this condition, continuous variables are needed to describe the neutron filter. Two different descriptions have been considered to achieve this:

(i) A variable thickness is assigned to each filter layer. The objective function is then minimised to find the optimal combination of thicknesses. This approach has the disadvantage that the order in which the materials are positioned is already fixed.

(ii) Each filter layer is described by a combination of several materials. In this approach, the aim is to find the optimal material concentrations in each layer.

Because of the additional degrees of freedom, it was decided to elaborate the second approach. This was attempted in the continuous filter model.

## 6.1 The continuous filter model

In the continuous filter model, the neutron filter is divided into a fixed number of layers. Each layer contains a mix of possibly all materials from a given material selection. These mixtures are homogeneous within each layer, but are allowed to vary between different layers. The composition of a filter is specified by an array $\boldsymbol{C}$ in which the element $c_{m,n}$ is equal to the relative concentration of material $m$ in layer $n$. In our model problem, the index $b$ is also added to distinguish between filters in different beam directions. For convenience, this subscript is left out for now. The elements $c_{m,n}$ take values between zero and one because they are defined as relative quantities. The relative material concentration is a fraction, which is defined as the amount of material $m$ inside the mixed layer with respect to the total amount that is present in the predefined slab of material $m$. Because these predefined slabs have variable sizes, the thickness of each layer can also vary in the continuous filter model.

In the filter transport calculation, transmission and reflection matrices are used. These matrices have been defined and determined for pure materials. In this new filter model, transmission and reflection matrices are required for mixed layers. Therefore, a new set of matrices is defined, denoted by $\tilde{\boldsymbol{T}}_{\boldsymbol{n}}$ and $\tilde{\boldsymbol{R}}_{\boldsymbol{n}}$, which can be used for a mixture in layer $n$. These matrices are obtained by taking linear combinations of the original matrices $\boldsymbol{T}_{\boldsymbol{m}}$ and $\boldsymbol{R}_{\boldsymbol{m}}$, which are specified for a single material $m$:

$$\tilde{\boldsymbol{T}}_{\boldsymbol{n}} = \boldsymbol{I} + \sum_{m=1}^{M} c_{m,n}(\boldsymbol{T}_{\boldsymbol{m}} - \boldsymbol{I}), \qquad \tilde{\boldsymbol{R}}_{\boldsymbol{n}} = \sum_{m=1}^{M} c_{m,n}\boldsymbol{R}_{\boldsymbol{m}}. \tag{6.1}$$

Here, $\tilde{\boldsymbol{T}}_{\boldsymbol{n}}$ and $\tilde{\boldsymbol{R}}_{\boldsymbol{n}}$ have slightly different expressions due to effect of void layers. If the sum of the material concentrations inside a layer is smaller than one, the remainder of this layer is treated as void. The transmission matrix of such a layer is equal to the identity matrix $\boldsymbol{I}$. Hence, $\tilde{\boldsymbol{T}}_{\boldsymbol{n}} = \boldsymbol{I}$ if all $c_{m,n}$ are zero. In the case of the reflection matrix, the expression reduces to $\tilde{\boldsymbol{R}}_{\boldsymbol{n}} = \boldsymbol{0}$ if the layer is empty.

The reason to use linear combinations of the material matrices can be explained by their definitions. The elements of the transmission matrices can be seen as probabilities that a neutron is transmitted from one group to another after passing this layer. Suppose a certain interaction probability is $T_1$ for material 1 and $T_2$ for material 2. If a layer consists of these two materials with relative fractions of $c_1$ and $c_2$, one could argue that the total probability that this interaction occurs in the mixed layer is $c_1 \cdot T_1 + c_2 \cdot T_2$. However, there is also a probability that neutrons interact with both materials. When more materials are added, new combinations of interactions are possible, which are not taken into account by this model. For this reason, the expressions in Equation 6.1 do not give an exact description of mixed layers, but they can be used as approximations.

The transmitted neutron fluxes through an arbitrary mixed layer have been calculated to demonstrate the accuracy of this approximation. As an example, a 10 cm thick slab which consists of 60% $^{27}$Al, 30% $^{28}$Si and 10% $^{32}$S (given by mass percentages) is used. The transmission matrix of this slab is calculated both directly in XSDRN and by taking a linear combination of the separate transmission matrices. A comparison between the two transmission matrices applied on a uniform input spectrum is shown in Figure 6.1. It can be seen that most group fluxes are approximated well. However, at some points in the fast energy region larger errors are visible.

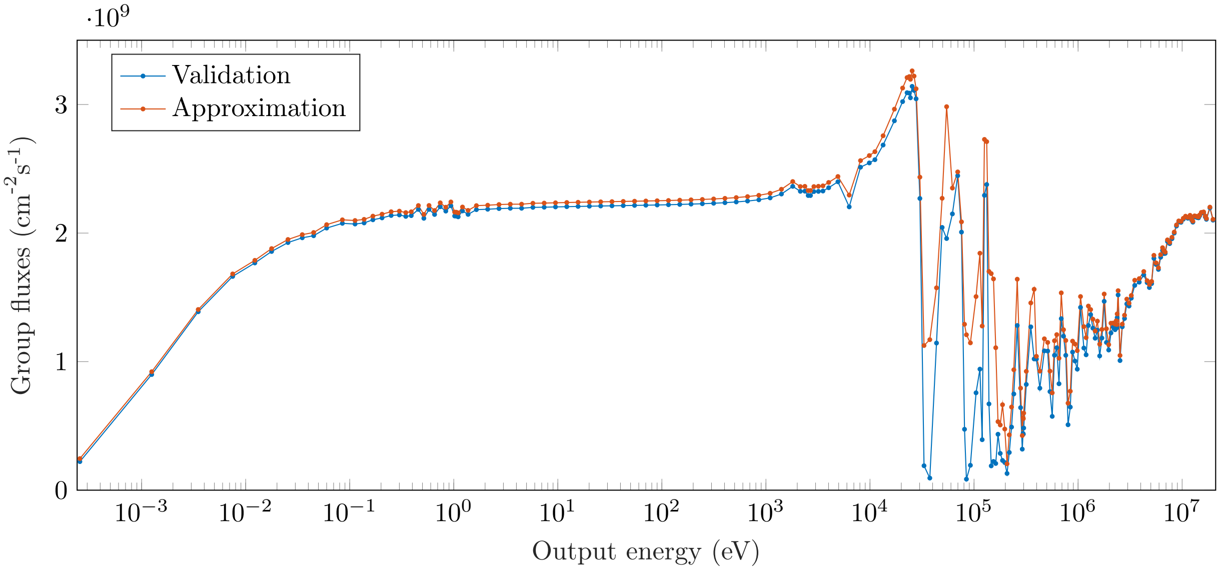

**Figure 6.1:** Validation of the approximated transmission matrix of a single mixed layer. The output spectra have been calculated by $\vec{\phi}_{out} = \boldsymbol{T}\vec{\phi}_{in}$. An input spectrum of $10^{12}$ neutrons cm$^{-2}$s$^{-1}$ is used with equal fluxes in each energy group. The transmission matrix of the validation was calculated in XSDRN by using a 10 cm thick layer of a material with a density of 2.53 g/cm$^3$ containing Al-27, Si-28 and S-32 with relative mass fractions of 0.6, 0.3 and 0.1 respectively. The material fractions with respect to their predefined slabs have been determined using the densities of the individual materials. Then, the transmission matrix of the approximation was calculated by taking the linear combination $\tilde{\boldsymbol{T}} = 0.58\boldsymbol{T}_{\text{Al}} + 0.33\boldsymbol{T}_{\text{Si}} + 0.12\boldsymbol{T}_{\text{S}}$.

The concept to use mixed material layers could give some troubles when building the filter in practice. Some materials can easily by combined like an alloy of metals, but other combinations might be less realistic. Another option to create such a layer in practice, is by using thin alternating layers. If the thickness of these layers is taken much smaller than $1/\Sigma_t$, the characteristics will be similar to a material mixture. This could be a way to implement the filters that are found by this model in a real treatment.

## 6.2 Gradient calculation

When the relative material concentrations $c_{m,n,b}$ from the new filter model are used as input variables, the calculation scheme becomes:

$$c_{m,n,b} \xrightarrow{\text{filter calculation}} \varphi_{g,b} \xrightarrow{\text{dose calculation}} D_{i,b} \xrightarrow{\text{cost function}} F$$

An expression for the gradient is needed for the optimisation algorithm. Using the chain rule, the gradient $\partial F/\partial c$ can be expressed as the product of the gradients of the three functions given above. Two of them are obtained easily by taking the derivatives of the analytical functions. First of all, the derivative of the cost function with respect to the dose contributions is determined. Using the same matrix notation that was defined in Section 5.2, this gradient becomes

$$\frac{\partial F}{\partial \boldsymbol{D}} = 2\boldsymbol{W}(\boldsymbol{D}\vec{t} - \vec{P})\vec{t}^{\,T}. \tag{6.2}$$

Secondly, the gradient of the dose calculation is given by

$$\left(\frac{\partial D_i}{\partial \varphi_g}\right)_b = A_0 t_0 d_{ig,b}, \tag{6.3}$$

where the elements of the dose transfer matrices $d_{ig}$ are multiplied by the beam area and treatment time.

The final gradient is less straightforward to evaluate. This is the derivative of the particle fluxes $\varphi_{g,b}$ with respect to the material concentrations $c_{m,n,b}$ following from the filter calculation. This calculation is performed by an iterative process instead of an explicit function. Therefore, we need to look into the transport model once more, which was formulated in Section 3.3.2. Now, the aim is to estimate how the particle fluxes at the exit of the filter are influenced by a change in filter composition.

Suppose the relative concentration of material $m$ in layer $n$ is increased by a small amount $\Delta c$ (Figure 6.2). Because of this, the transmission and reflection matrices of this particular layer are changed. According to Equation 6.1 they are replaced as follows,

$$\begin{aligned} \tilde{\boldsymbol{T}}'_{\boldsymbol{n}} &\to \tilde{\boldsymbol{T}}_{\boldsymbol{n}} + \Delta c(\boldsymbol{T}_{\boldsymbol{m}} - \boldsymbol{I}), \\ \tilde{\boldsymbol{R}}'_{\boldsymbol{n}} &\to \tilde{\boldsymbol{R}}_{\boldsymbol{n}} + \Delta c \boldsymbol{R}_{\boldsymbol{m}}. \end{aligned}$$

The particle fluxes entering layer $n$ are given by $\vec{\phi}^{+}_{n-1}$ and $\vec{\phi}^{-}_{n}$, which are known when the filter calculation is done. The particle fluxes leaving this layer are calculated by applying the new transmission and reflection matrices on these incoming fluxes. The change in outgoing fluxes $\Delta\vec{\phi}^{+}_{n}$ and $\Delta\vec{\phi}^{-}_{n-1}$ can then be expressed as

$$\Delta\vec{\phi}^{+}_{n} = \Delta c(\boldsymbol{T}_{\boldsymbol{m}} - \boldsymbol{I})\vec{\phi}^{+}_{n-1} + \Delta c \boldsymbol{R}_{\boldsymbol{m}} \vec{\phi}^{-}_{n} \equiv \vec{S}^{+}_{n}, \tag{6.4}$$

$$\Delta\vec{\phi}^{-}_{n-1} = \Delta c(\boldsymbol{T}_{\boldsymbol{m}} - \boldsymbol{I})\vec{\phi}^{-}_{n} + \Delta c \boldsymbol{R}_{\boldsymbol{m}} \vec{\phi}^{+}_{n-1} \equiv \vec{S}^{-}_{n-1}. \tag{6.5}$$

These $\Delta\vec{\phi}^{+}_{n}$ and $\Delta\vec{\phi}^{-}_{n-1}$ are modelled as perturbation sources $\vec{S}^{+}_{n}$ and $\vec{S}^{-}_{n-1}$ at the boundaries of layer $n$. The transport model based on matrix multiplication is used to calculate the propagation of these perturbations through the entire filter. This is done similarly as described by Equation 3.6, but now the operators $\tilde{\boldsymbol{T}}_{\boldsymbol{i}}$ and $\tilde{\boldsymbol{R}}_{\boldsymbol{i}}$ are working on the change in flux $\Delta\vec{\phi}_i$ instead of the particle flux $\vec{\phi}_i$ itself. Also, a source term $\vec{S}_i$ is added to include the perturbation sources $\vec{S}^{+}_{n}$ and $\vec{S}^{-}_{n-1}$. On all other spatial intervals, $\vec{S}_i$ is taken zero. Vacuum boundary conditions are used at both ends of the filter. The system is then described by the following two equations, where the subscript $i$ indicates the spatial interval and the iteration number is given by $k$:

$$\begin{cases} \Delta\vec{\phi}^{+}_{i,k} = \tilde{\boldsymbol{T}}_{\boldsymbol{i}} \Delta\vec{\phi}^{+}_{i-1,k} + \tilde{\boldsymbol{R}}_{\boldsymbol{i}} \Delta\vec{\phi}^{-}_{i,k-1} + \vec{S}^{+}_{i} & \Delta\vec{\phi}^{+}_{0} = \vec{0} \\ \Delta\vec{\phi}^{-}_{i,k} = \tilde{\boldsymbol{T}}_{\boldsymbol{i+1}} \Delta\vec{\phi}^{-}_{i+1,k} + \tilde{\boldsymbol{R}}_{\boldsymbol{i+1}} \Delta\vec{\phi}^{+}_{i,k} + \vec{S}^{-}_{i} & \Delta\vec{\phi}^{-}_{N} = \vec{0} \end{cases} \tag{6.6}$$

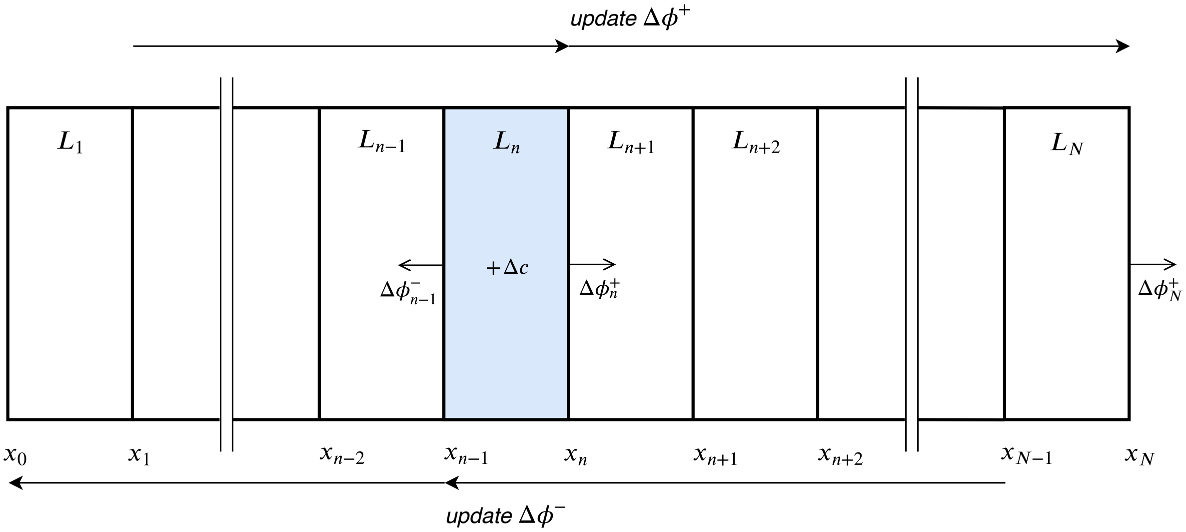

**Figure 6.2:** Schematic overview of the transport model by matrix multiplication, in which the gradient $\frac{\partial\varphi}{\partial c}$ can be approximated. A change in material concentration $\Delta c$ in one of the filter layers is modelled by two perturbation sources $\vec{S}^+_n$ and $\vec{S}^-_{n-1}$ at the boundaries of this layer. The perturbations are propagated by transmission and reflection as described by the system of equations in 6.6. Iterations are performed in the directions of the arrows to estimate $\Delta\vec{\phi}^+_N$ at the exit of the filter.

Iterations are performed by updating $\Delta\vec{\phi}^+_i$ from $i = 1$ to $i = N$, followed by updating $\Delta\vec{\phi}^-_i$ from $i = N - 1$ back to $i = 0$. In the first iteration, the first $n - 1$ points can be skipped because they are not affected by any of the sources. As the perturbation sources are expressed in $\Delta c$, all values for $\Delta\vec{\phi}_i$ are calculated in terms of $\Delta c$ as well. This starts with a linear component and each time the fluxes have passed the perturbed layer again, a higher-order approximation can be made. As a result, the flux change at the exit of the filter takes the form $\Delta\vec{\phi}^+_N = \vec{f}_1\Delta c + \vec{f}_2(\Delta c)^2 + \ldots$ . Then, the derivative is given by

$$\frac{\partial\varphi_g}{\partial c_{m,n}} = \lim_{\Delta c\to 0}\frac{\Delta\vec{\phi}^+_N}{\Delta c} = \lim_{\Delta c\to 0}\frac{1}{\Delta c}\left(\vec{f}_1\Delta c + \vec{f}_2(\Delta c)^2 + \ldots\right) = \vec{f}_1.$$

Hence, only a first-order approximation of $\Delta\vec{\phi}^+_N$ is used to estimate the gradient. All higher-order terms of $\Delta c$ are neglected. This is realized by using the original matrices $\tilde{\boldsymbol{T}}_{\boldsymbol{n}}$ and $\tilde{\boldsymbol{R}}_{\boldsymbol{n}}$ in the perturbed layer without the change in concentration taken into account. This way, a first-order approximation of $\Delta\vec{\phi}^+_N$ and an estimation of the gradient are found after the final iteration. Approximately 20 iterations were needed until convergence when a filter of 25 layers was used.

In principle, this calculation is relatively fast because of the efficient use of sparse matrix multiplications. However, this gradient needs to be calculated with respect to each material concentration in each filter layer. Depending on the number of materials and filter layers, this can typically add up to more than a thousand independent variables $c_{m,n,b}$ and the same number of perturbation calculations. Because of this, the computation of the gradient is by far the most time-consuming part of the optimisation. Gradient descent algorithms do not necessarily have to use exact values for the gradient. An approximation can be sufficient to lead the solver towards a minimum. Therefore, it is beneficial to use a small number of iterations in the gradient calculation. After only 5 iterations the approximation seems to be reasonably accurate. This is shown for two different materials in Figure 6.3. Here, the approximations of the gradient have been compared with finite difference estimations. Small errors are acceptable in this approximation, if the computation time is reduced significantly.

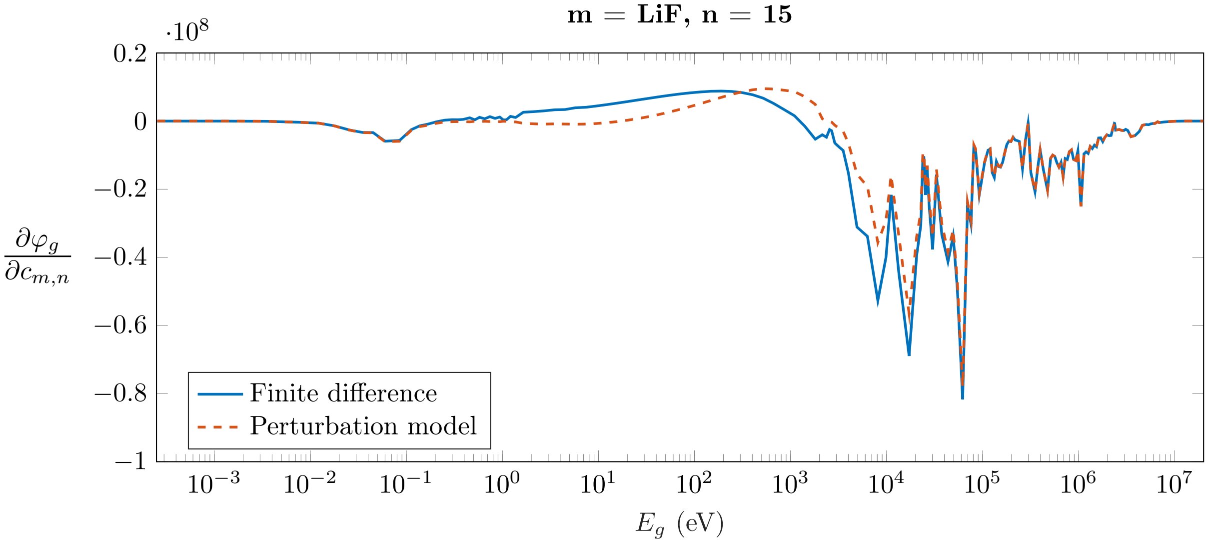

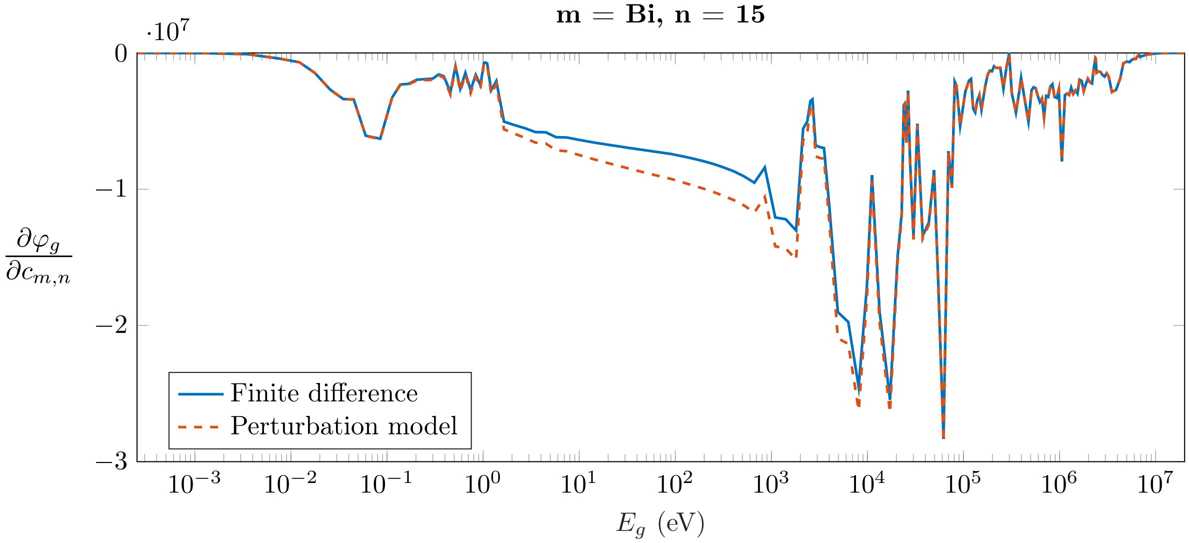

**Figure 6.3:** Comparison of the derivatives $\partial\varphi_g/\partial c_{m,n}$ approximated by the perturbation model and by finite differences. This was done for lithium fluoride and bismuth, both in layer 15 which is located in the middle of the neutron filter. The approximation in the perturbation model was obtained with 5 iterations. The finite difference calculation was done with $\Delta c = 10^{-8}$ and is assumed to give an exact estimation of the gradient. For most energies, the approximation seems very accurate. Both gradients were calculated at the starting point of the algorithm, which is $c = 0.05$ for each layer and each material.

## 6.3 A gradient descent algorithm applied on the model problem

### 6.3.1 Details of the algorithm

The interior-point algorithm in Matlab was used to find the optimum filter compositions in the model problem. Neutron filters were placed in each of the five selected beam directions (see Figure 5.1). Each filter was described by the continuous filter model allowing for 12 different materials in 25 layers per filter, which adds up to 1500 independent material concentrations $c_{m,n,b}$. These parameters were constrained by $\sum_{m=1}^{12} c_{m,n,b} \leq 1$ to restrict the maximum amount of materials in each filter layer $n$. Also, each individual concentration was bound by $0 \leq c_{m,n,b} \leq 1$. The starting point was chosen at $c_{m,n,b} = 0.05$ for all $m$, $n$ and $b$, which means equal concentrations of each material were added in each layer.

A standard step in the optimisation consists of an evaluation of the objective function (Equation 5.1) and an approximation of the gradient. The evaluation of the objective function takes about 3 CPU minutes. The gradient approximation was included as described in Section 6.2. Here, 5 iterations were used to estimate $\partial\varphi_g/\partial c_{m,n}$. This resulted in a calculation time of 64 CPU minutes to determine the gradient of the objective function with respect to all 1500 input variables. The interior-point algorithm also has the option to include the Hessian. However, this would increase the calculation time of each step even more and it could be doubted if the second-order derivatives would be accurate enough if they are based on approximated first-order derivatives. Therefore, no Hessian was included in the algorithm.

The stopping criteria of the algorithm are given by the so-called tolerance limits. These are set for both the input variables $c$ and the objective function $F$. When the solver is close to a minimum, the algorithm is terminated after iteration $k$ if $|c_k - c_{k+1}|$ has become smaller than the step tolerance or if $|F(c_k) - F(c_{k+1})|$ has become smaller than the function tolerance. The step tolerance is set to $10^{-5}$, which is expected to provide a sufficiently accurate description of the material concentrations. The function tolerance is set to $10^5$ since no significant differences in dose distributions are observed for this order of magnitude.

### 6.3.2 Results

The algorithm stopped after 163 function evaluations, because the step size had become smaller than the step tolerance. This took approximately 36 hours on 5 cores. The optimised material concentrations for all five neutron filters are shown in Figure 6.4. Many of the relative concentrations turned out to be close to either zero or one. This means that most filter layers could be built from pure materials, which is beneficial for practical reasons. Nevertheless, one should keep in mind that even small concentrations of certain materials can influence the output spectrum. Although each filter has its own unique composition, some similarities can be observed. The first layers are often composed of Al, $AlF_3$ and sometimes LiF, which seems to work efficiently as a combined moderator. Some other repeated patterns are Al-S-$B_4C$ and $AlF_3$-Ni-Al at the end of the filters. Boron-10 is used as thermal neutron absorber and seems to appear at arbitrary locations in each filter. The other possible neutron absorber cadmium is not used in any of these filters. Not so many gamma shields are present in the optimised compositions. Only a single layer of lead can be found at the end of two filters.

The minimum cost of $F = 2.38 \cdot 10^7$ that was found in this optimisation is not necessarily a global minimum. A few more optimisation runs have been performed for different starting points. In these optimisations, other minima were found. The second best solution for example, was found by using $c_{m,n,b} = 0.01$ for all material concentrations as starting point. The resulting minimised cost value was $F = 2.47 \cdot 10^7$. Some of the optimised filters from this second best solution are shown in Figure 6.5. These filter compositions are completely different compared to the previous solution. Many layers are composed of nickel instead of aluminium, and small amounts of bismuth and cadmium are present as well. Despite these large differences in filter composition, the resulting dose distributions are almost similar. These results demonstrate that the problem is not convex and multiple local minima exist. There might be many different filter designs which lead to similar results.

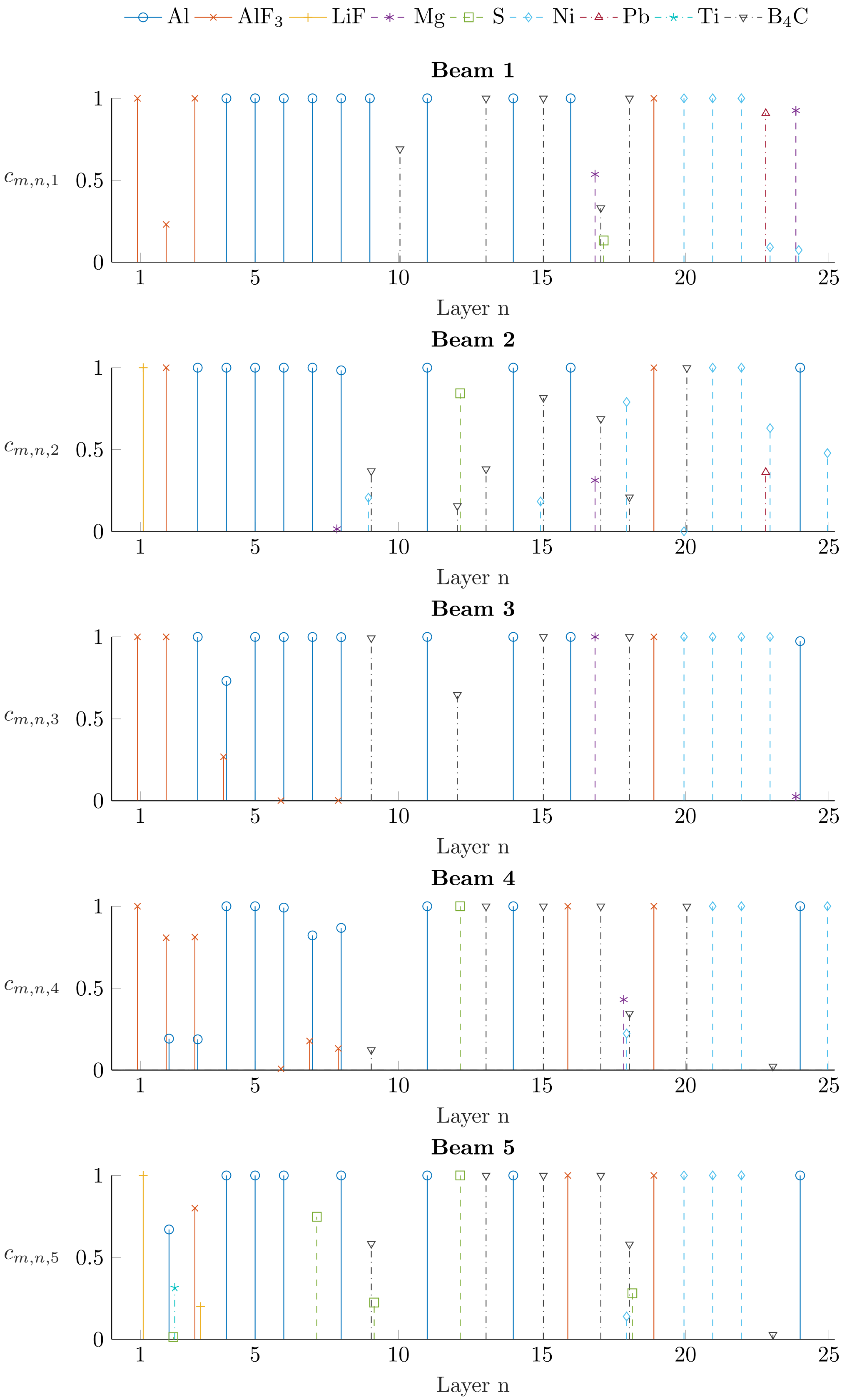

**Figure 6.4:** Optimised values for the material concentrations that were found using $c_{m,n,b} = 0.05$ as starting point.

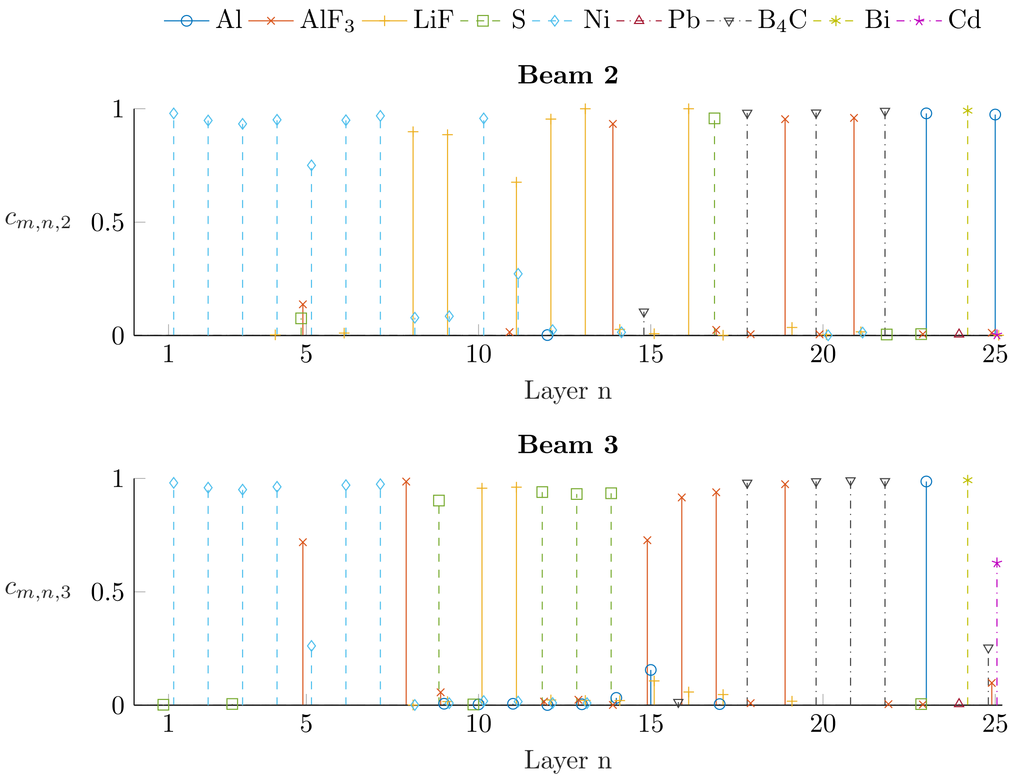

**Figure 6.5:** Two of the optimised filters that were found using $c_{m,n,b} = 0.01$ as alternative starting point.

The filtered and collimated output spectra of the best found solution are shown in Figure 6.6. The filters have removed most of the thermal and fast neutrons. The fraction of epithermal neutrons is between 0.93 and 0.96 in each beam. The total beam intensities are between 2.9 and $3.7{\cdot}10^9$ neutrons $\text{cm}^{-2}\text{s}^{-1}$. With these neutron fluxes, the desired dose could be delivered within a total treatment time of 3.2 hours. This is a reasonable time if the treatment is divided over several fractions.

The resulting dose distribution in the brain phantom is given in Figure 6.7. The brainstem received a maximum dose of 11 Gy-Eq, which is far below the imposed dose constraint. In the tumour, a mean dose of 56 Gy-Eq is delivered, which is close to the prescribed dose of 60 Gy-Eq. However, the algorithm has not succeeded in delivering a uniform dose distribution inside the tumour. The wide dose range between 43 and 74 Gy-Eq would probably not be acceptable in practice. This problem is caused by the OAR which is touching the tumour region. Possibly, the uniformity of the tumour dose can be improved somewhat by further adjustment of the voxel weights. Another option is to irradiate the tumour from different angles. For simplicity, all beam directions in the model problem were selected in the same plane. Additional beams could be added orthogonal to the $xy$-plane to contribute to a more uniform dose distribution.

An important aspect in beam optimisation is the trade-off between beam quality and intensity. In fact, this algorithm is only optimising the beam qualities by looking for the best possible relative dose distribution. Using the presumed source intensity of $5 \cdot 10^{12}$ neutrons $\text{cm}^{-2}\text{s}^{-1}$ at the beam tube entrance, the demanded treatment time turned out to be realistic. If a weaker source were used, this could have caused some difficulties to deliver the dose within a reasonable time. In the current algorithm, the total number of layers per filter $N$ can be varied to influence the filtered beam intensities. By decreasing this parameter, it can be expected that more neutrons are transmitted through the filters. This way, higher neutron fluxes can be obtained at the cost of some of the beam quality. Alternatively, the algorithm can be improved by using a new objective function in which long treatment times are penalised. In that case, a trade-off between beam quality and intensity is made regardless of the number of filter layers.

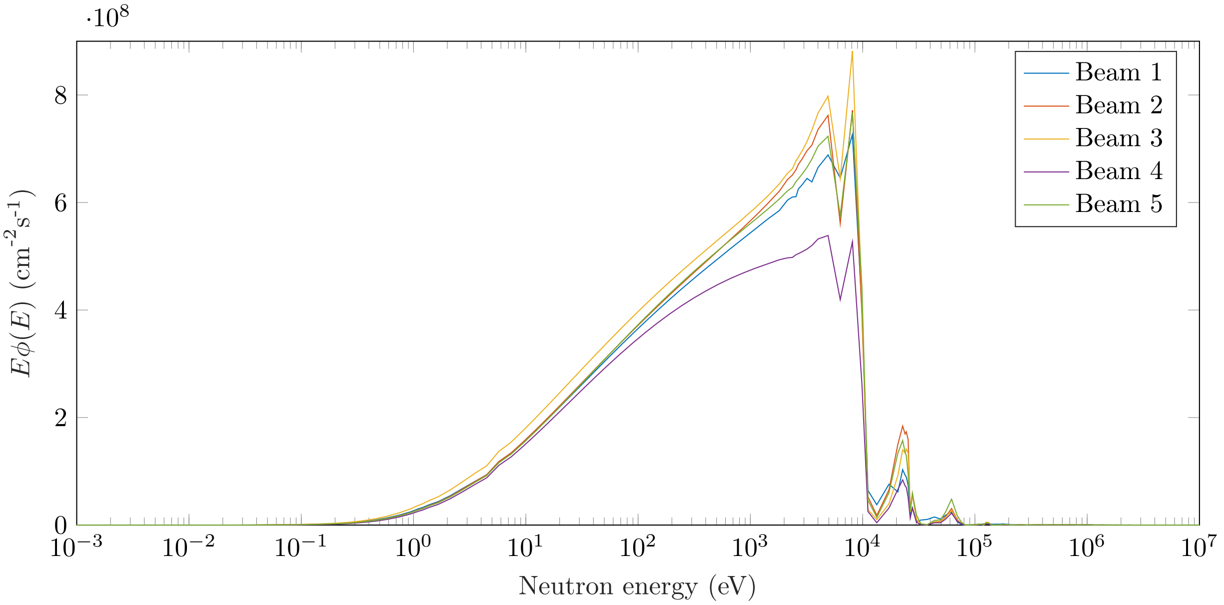

**Figure 6.6:** Energy spectra of the filtered neutron beams at an angle of $\mu = 0.98$ shown as $E\phi(E)$ for the optimum filter compositions. All beams consist predominantly of epithermal neutrons. Also, two lower peaks in the fast energy region are visible around 23 keV and 62 keV in each beam.

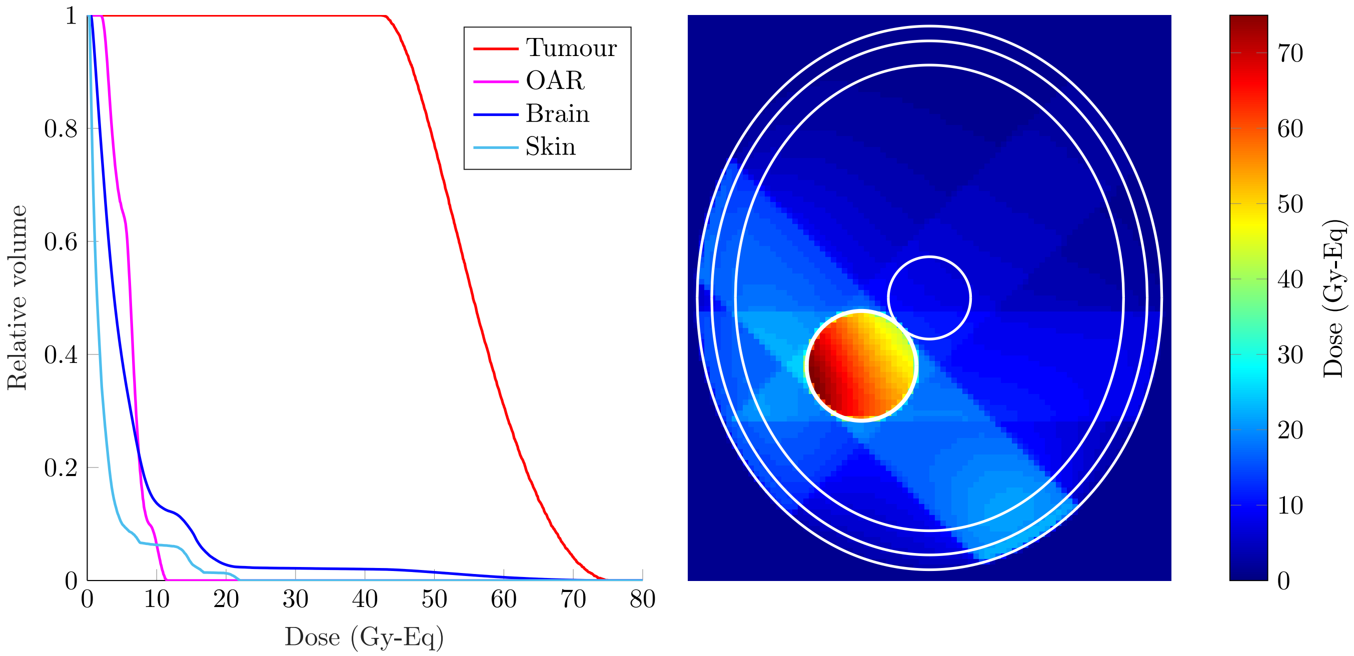

**Figure 6.7:** The optimised dose distribution shown in a cumulative dose volume histogram (left) and in the $xy$-plane of the brain phantom (right). The treatment times per beam are $t_1 = 0.66$ h, $t_2 = 0.56$ h, $t_3 = 0.58$ h, $t_4 = 1.17$ h and $t_5 = 0.24$ h.

# 7 | Filter Optimisation by a Genetic Algorithm

Optimisation methods based on gradient descent come with some disadvantages. First of all, it is not always possible to find an expression for the gradient of complicated objective functions. In our filter problem, the gradient of the cost function can be approximated, but relatively long computation times are needed to evaluate the gradient at each point. Furthermore, these methods involve the risk of getting trapped in a local minimum. If the solution space is large, it requires many optimisation runs from different starting points before a satisfactory solution is found.

Some of these issues can be solved by a category of alternative optimisation algorithms. These algorithms use completely different approaches compared to gradient methods and can be classified as natural or probabilistic methods. Some of them include the genetic algorithm (Holland, 1975), simulated annealing (Kirkpatrick et al., 1983) and particle swarm optimisation (Parsopoulos and Vrahatis, 2002). These methods are inspired on processes in nature. They all use their own techniques to generate new points in the solution space by applying operators on possible solutions. This way, it is possible to move statistically towards more optimal solutions. These algorithms do not require taking cost function derivatives and can thus deal with discrete variables and non-continuous objective functions [48]. In this thesis, it was decided to look further into genetic algorithms and investigate how these could be applied on filter optimisation.

## 7.1 The genetic algorithm

Genetic algorithms are based on the principles of genetics and natural selection. Instead of iterations, these algorithms work with so-called generations. Each generation is composed of a group of solutions, which is called a population. The aim is to let these populations evolve under specified selection rules to a state that minimises the cost function.

Each candidate solution is encoded by an array of fixed length. The algorithm starts with randomly generating an initial population which consists of a predefined number of candidate solutions. Then, the objective function is evaluated for each solution in this population. Based on the individual scores or cost values, a new population is created in the next generation. Normally, a specified number of elite solutions is chosen, which are the best solutions of the population. The elite solutions are always copied to the next generation. The remainder of the new population is made up by newly created solutions. This is done by first selecting two parent solutions from the old population and then apply an operator on them to generate two offspring solutions. This process is repeated until the new population contains as many individuals as the initial population. This way, the population size remains unchanged during the optimisation.

The selection of parent solutions can be done in various ways. One of the commonly used techniques is the roulette wheel selection, in which a solution is chosen with a probability proportional to its fitness. In case of a minimisation problem, the fitness can be defined as the inverse of the cost function. Another option is to select solutions based on tournament. In tournament selection, a specified number of solutions is chosen at random and then the best individual out of that set is selected as parent solution. The tournament selection has better or equivalent convergence and computational time properties compared to any other selection method that exists in literature [49].

The crossover and mutation operators are applied on the selected parent solutions to create offspring solutions. Crossover recombines features of the selected candidate solutions. This operator can be defined in many different ways. For our application, we assume that each offspring solution is constructed by an array receiving half of its elements from parent 1 and the other half from parent 2. The selection of these elements is performed randomly for each crossover operation. By repeatedly creating new combinations of favourable elements, it can be expected that superior candidate solutions appear during the optimisation.

In the mutation operation, a number of elements from the parent solutions is replaced by random values. This often leads to worse solutions, but sometimes a significant improvement can occur by coincidence. Mutation is equivalent to a random search. When the optimisation is stagnating and the set of solutions becomes homogeneous at a certain point, the mutation operation can insert more diversity in the population. This way, it can prevent the algorithm from getting trapped in a local minimum. Figure 7.1 shows an example of the crossover and mutation operations on candidate solutions composed of eight integers. Which of these two operations is applied, depends on the crossover probability $p_c$ and the mutation probability $p_m$. These parameters are specified beforehand. A value of $p_c = 0.7$ is typically used for crossover [50]. If crossover and mutation are the only possible recombination methods, the mutation probability is taken $p_m = 1 - p_c$.

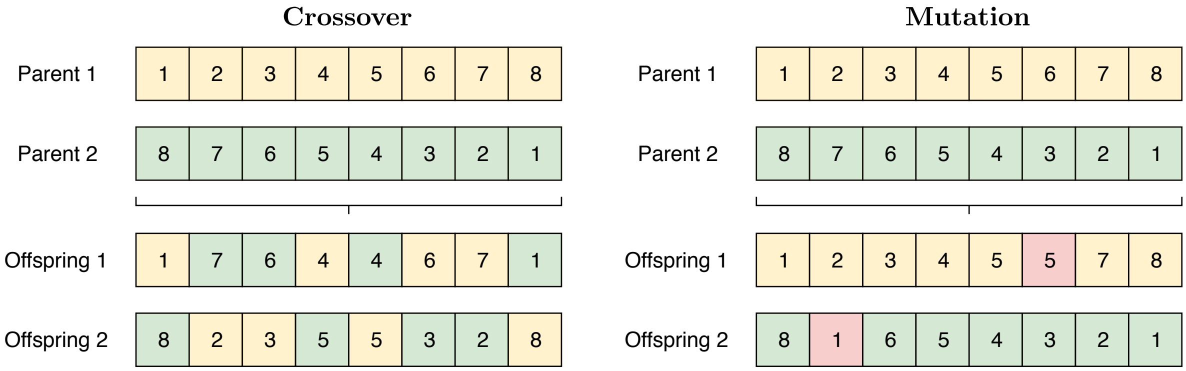

**Figure 7.1:** Schematic representations of the crossover and mutation operations. Both operators use two parent solutions as input and create two offspring solutions as output, which are added to the new population.

This cycle of creating new populations and evaluating the objective function for all individuals is repeated for each generation. Because of the elite solutions, the best solution in each generation is at least equal to or better than the best solution from the previous generation. Furthermore, the average fitness of a population tends to increase over the course of generations, which is proven by the schema theorem [50]. As a stopping criteria, the algorithm could be terminated if the optimum function value does not improve for a specified number of generations. However, this could be problematic because of the stochastic character of the algorithm. The fitness of a population might remain stable for a number of generations before a superior solution appears. An alternative is to simply terminate the algorithm after a specified number of generations and then take the best solutions in the final population. A typical number of generations for a genetic algorithm can range from 50 to over 500 [51].

## 7.2 A genetic algorithm applied on the model problem

A genetic algorithm was used to determine the optimum neutron filters in the model problem. Since this optimisation method can handle integer variables, there was no need to use the continuous filter model, in which mixed layers are approximated. Instead, all filters were modelled more realistically by layers of pure materials. Each neutron filter was encoded by an array of 25 integers representing the filter layers. The integer variables were allowed to range from 0 to 12, where each value corresponds to a specific material. Zeros were used to model void layers. Combining all five neutron filters, this gave a total of 125 integers in each candidate solution.

### 7.2.1 Details of the algorithm

Many standard versions of the genetic algorithm are available, such as the *ga* function in the Global Optimisation Toolbox of Matlab. In this thesis, a new algorithm was written based on this function in Matlab with some minor modifications to make it suitable for integer variables. Also, customized crossover and mutation functions were added. These functions are equivalent to the representations in Figure 7.1. A flow chart including all steps and optimisation parameters of the genetic algorithm is shown in Figure 7.2. Also, a complete description of the algorithm can be found in the Appendix. Using these settings, the calculation takes about 8.4 CPU hours for each generation. This is mainly caused by the large population size.

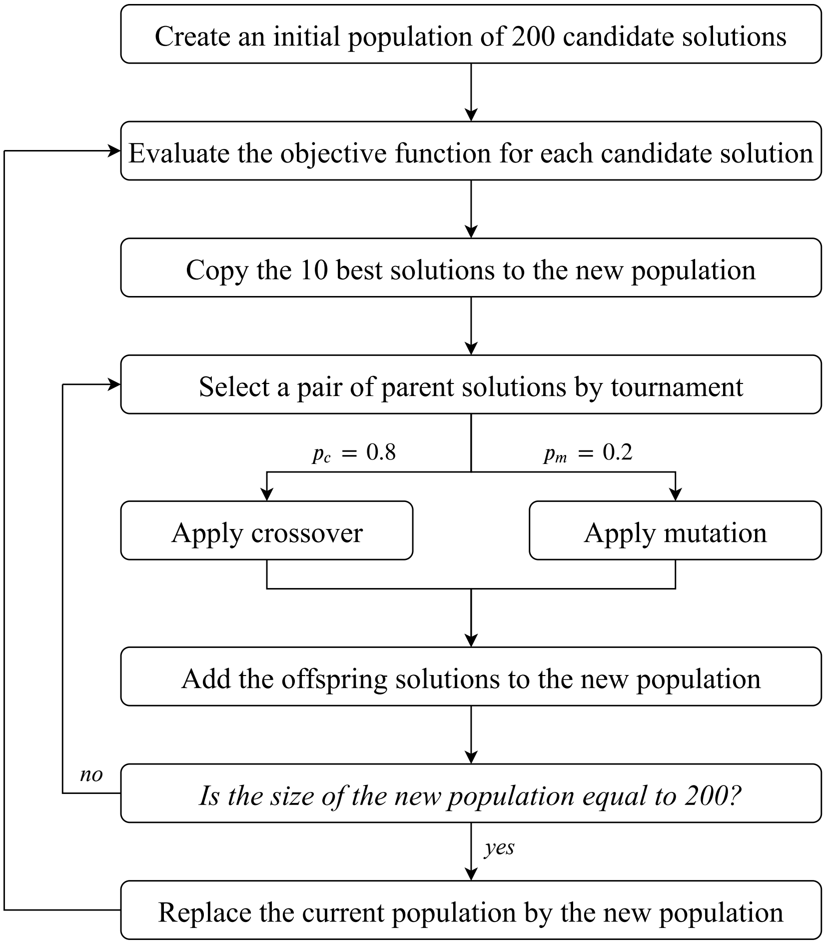

**Figure 7.2:** Flow chart of the genetic algorithm. A population size of 200 is used. The elite count is defined as 5% of the total population, which means the 10 best solutions in each generation are guaranteed to survive to the next generation. Selection is performed by tournament using a tournament size of four solutions. The crossover and mutation operators are taken equivalent to the representations in Figure 7.1. In the mutation operation, it is decided to affect 10% of all variables in a solution.

### 7.2.2 Results

Several optimisation runs have been performed for varying crossover and mutation probabilities. In all cases, the algorithm was terminated after 70 generations because the optimum solution did not seem to improve anymore. The cost value of the best solution that was found in each generation is shown in Figure 7.3. After

20 generations, one of the populations contained a solution similar to the gradient descent optimum. Some further decrease in the minimum cost was achieved in the subsequent generations. The best solution was found for a crossover probability of $p_c = 0.8$. In this section, the results are discussed for this solution.

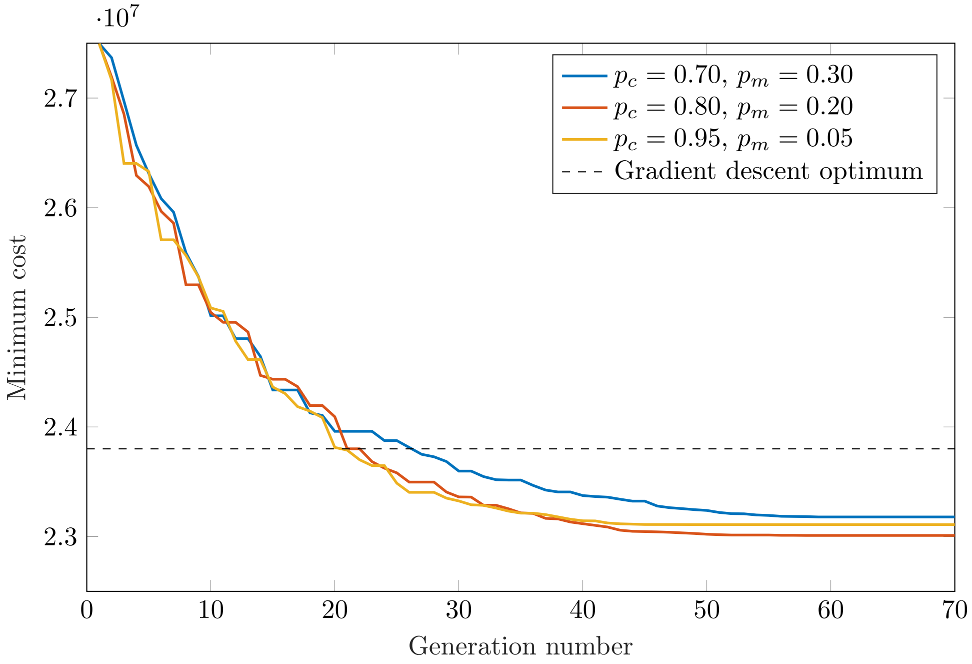

**Figure 7.3:** Performance graphs for different crossover and mutation probabilities. All optimisation runs used the same initial population. The minimum cost value is given for each generation. The best solution found in the gradient descent algorithm is indicated by the dashed line.

The optimised filter compositions are given in Table 7.1. The neutron beam in the fifth beam direction was not used in this configuration. The other four neutron filters contain large amounts of Al and $AlF_3$. Also, the thermal neutron absorber $B_4C$ appears in many layers. Overall, lots of varieties in material composition can be observed between the different filters. This is probably the case because all solutions have originated from a randomly generated initial population. As a result, the various materials were present at random positions from the beginning. This is in contrast with the homogeneous filter layers that were used as a starting point in the gradient descent algorithm. In that case, more similarities were visible between the filters in the optimum configuration.

Figure 7.4 shows the energy spectra of the filtered neutron beams. Although all beams have high epithermal neutron fractions between 0.94 and 0.98, some clear differences are visible between the individual spectra. Filter 3 for example, contains the largest number of boron layers and therefore relatively few spectrum shifters. In the resulting output beam, it can be seen that the low-energy spectrum is attenuated more, while higher intensities are obtained between 1 and 11 keV. Furthermore, this solution shows how two completely different filter compositions (filter 1 and 4) generate almost similar output spectra. This confirms the notion that many different filter designs can possibly lead to similar results.

The total beam intensities are between $1.4 \cdot 10^9$ and $2.2 \cdot 10^9$ neutrons $cm^{-2}s^{-1}$. This is somewhat weaker than the output fluxes that were found in the gradient descent algorithm. As a consequence, a longer treatment time of 5.4 hours is needed to deliver the desired dose. The delivered dose distribution and the corresponding dose volume histogram are shown in Figure 7.5. As a reference, the optimum dose distribution obtained in the gradient descent algorithm is given by the dashed lines. There is a close resemblance between the two dose distributions. The dose uniformity in the tumour shows some minimal improvements in the genetic algorithm result. Using this filter configuration however, a somewhat higher maximum dose is delivered in the OAR.

**Table 7.1:** Optimised neutron filters in beam direction 1 to 4.

| **Layer #** | **Filter 1** | **Filter 2** | **Filter 3** | **Filter 4** |
|---|---|---|---|---|
| 1 | LiF | Si | Mg | Al |
| 2 | Si | S | Al | Si |
| 3 | Al | Al | $B_4C$ | $B_4C$ |
| 4 | Bi | S | $B_4C$ | $B_4C$ |
| 5 | $AlF_3$ | $B_4C$ | Ni | Al |
| 6 | Al | Ni | LiF | Ti |
| 7 | LiF | LiF | Ni | $AlF_3$ |
| 8 | - | $AlF_3$ | $B_4C$ | $AlF_3$ |
| 9 | - | $B_4C$ | S | $AlF_3$ |
| 10 | $B_4C$ | $B_4C$ | $B_4C$ | LiF |
| 11 | Al | Al | Al | Al |
| 12 | S | Si | Al | Bi |
| 13 | Al | Al | $B_4C$ | $B_4C$ |
| 14 | $AlF_3$ | $B_4C$ | $B_4C$ | $B_4C$ |
| 15 | $B_4C$ | Al | $B_4C$ | Ni |
| 16 | Bi | Al | Al | S |
| 17 | Al | Al | Al | Al |
| 18 | Al | Al | $AlF_3$ | $B_4C$ |
| 19 | $B_4C$ | S | $AlF_3$ | $B_4C$ |
| 20 | $B_4C$ | Ni | $B_4C$ | Bi |
| 21 | $AlF_3$ | Al | $AlF_3$ | Mg |
| 22 | Mg | LiF | LiF | Mg |
| 23 | Al | Mg | Si | LiF |
| 24 | Mg | LiF | Ni | LiF |
| 25 | $AlF_3$ | Ni | $AlF_3$ | Cd |

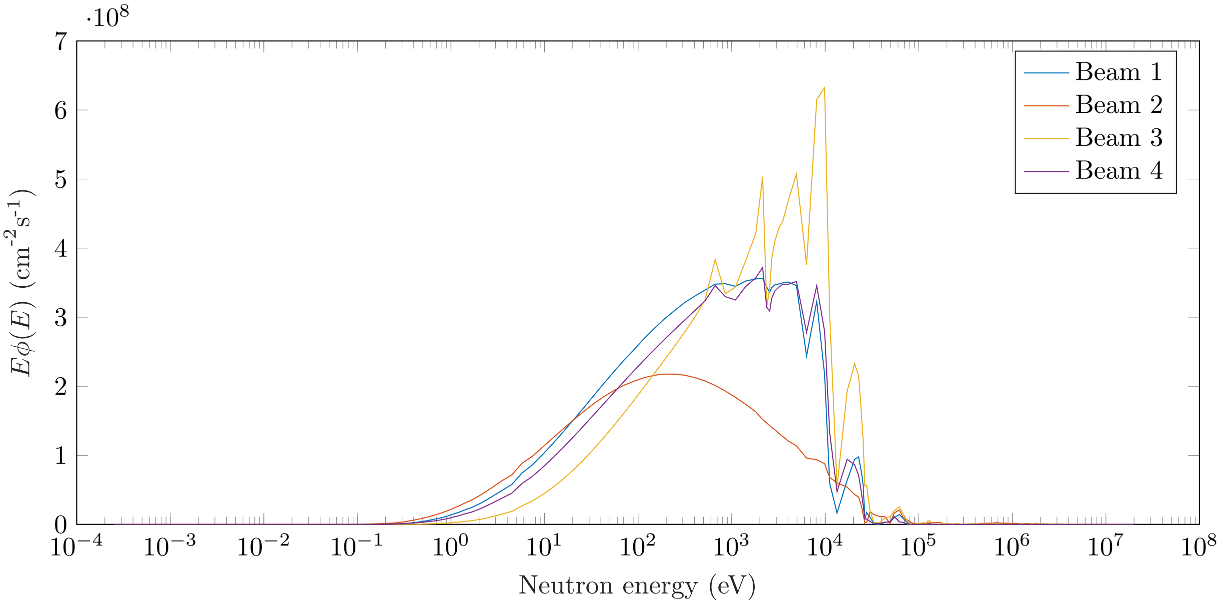

**Figure 7.4:** Energy spectra of the filtered neutron beams at an angle of $\mu = 0.98$ shown as $E\phi(E)$ for the optimum filter compositions. All beams consist predominantly of epithermal neutrons. The integrated fluxes for each beam are $\varphi_1 = 2.1 \cdot 10^9$, $\varphi_2 = 1.4 \cdot 10^9$, $\varphi_3 = 2.2 \cdot 10^9$ and $\varphi_4 = 2.0 \cdot 10^9$ neutrons cm$^{-2}$s$^{-1}$.

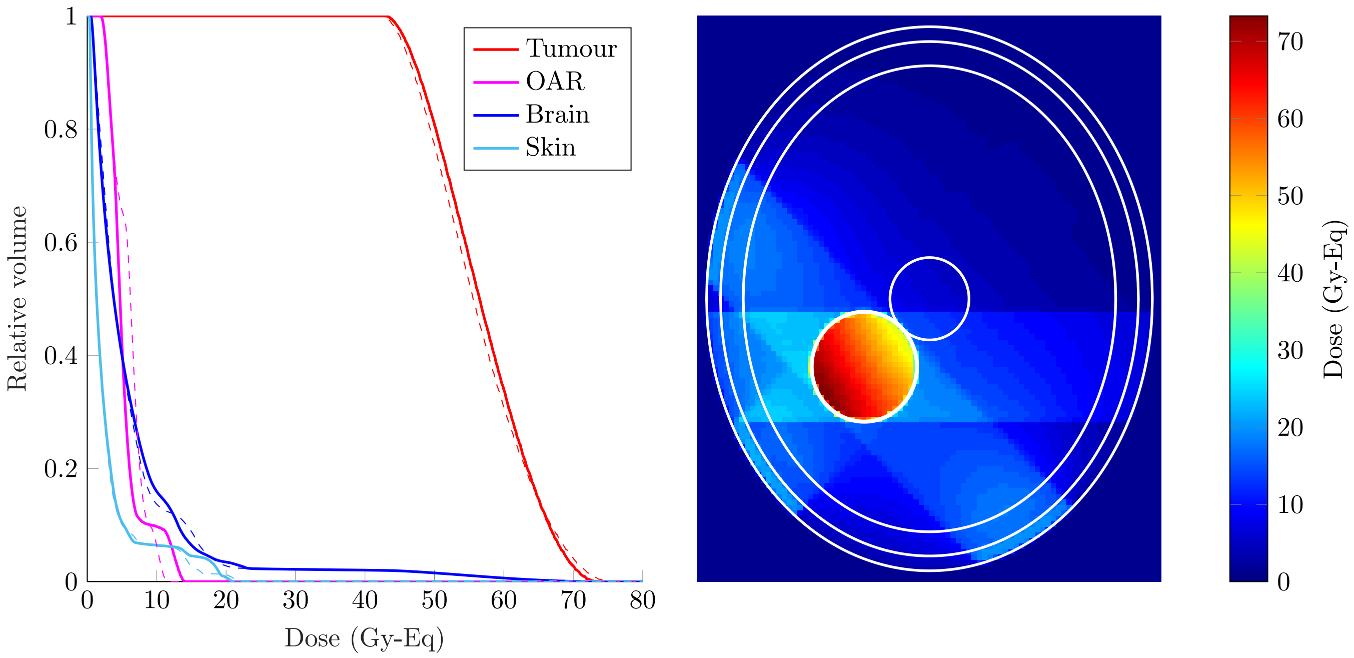

**Figure 7.5:** The optimised dose distribution shown in a cumulative dose volume histogram (left) and in the $xy$-plane of the brain phantom (right). As a comparison, the optimum distribution that was obtained in the gradient descent algorithm is indicated by the dashed lines in the cumulative dose volume histogram. The treatment times per beam are $t_1 = 1.74$ h, $t_2 = 0.19$ h, $t_3 = 1.56$ h, $t_4 = 1.88$ h and $t_5 = 0.00$ h.

**Table 7.2:** Comparison of the optimum treatment characteristics found in both algorithms.

| | **Gradient algorithm** | **Genetic algorithm** |
|---|---|---|
| Minimum cost | $2.38 \cdot 10^7$ | $2.29 \cdot 10^7$ |
| Mean tumour dose | 56.3 Gy-Eq | 56.8 Gy-Eq |
| $D_{98\%}$ in tumour | 44.2 Gy-Eq | 44.8 Gy-Eq |
| $D_{2\%}$ in tumour | 71.7 Gy-Eq | 70.5 Gy-Eq |
| $D_{2\%}$ in OAR | 10.7 Gy-Eq | 13.1 Gy-Eq |
| Total treatment time | 3.2 h | 5.4 h |

Some of the optimum treatment characteristics that were found in both algorithms have been compared and summarised in Table 7.2. Using the current objective function, the genetic algorithm result is considered as a better solution. Obviously, this is arguable and the objective function could be modified if one wishes to prioritise other aspects, such as the treatment time. This parameter could be implemented as an additional penalisation in the cost function.

Another remarkable result was observed regarding the dose components that are present in the optimum dose distribution. Almost 20% of all dose received by the tumour is delivered by gamma rays. From theory, one would expect the optimised filters to remove most of the photons, since they deliver a non-selective dose affecting all tissues. This was confirmed by some preliminary optimisations, in which only a single beam was used to irradiate the tumour. In that case, gamma shielding materials were present at the end of most optimised filters. However, this did not happen in the multiple beam geometry. In the best known solution, only a few layers of bismuth are used in two of the optimised filters (see Table 7.1). Also in the gradient descent optimum, no more than two layers of lead can be found in all filters (see Figure 6.4). In the specific case of the model problem, it seems extremely complicated to deliver the desired dose purely by neutron capture reactions. Apparently, better results can be obtained if some of the gamma rays are transmitted through the filters and therefore gamma shields are not always used.

Finally, a comparison can be made between the computation times of both algorithms. In the genetic algorithm, 21 generations were required to arrive at a result equivalent to the gradient descent optimum. This took about 35 hours as the calculation was running on 5 cores. This is comparable to the computation time of the gradient descent algorithm. In that algorithm, most time was spent approximating the gradient with respect to all possible material concentrations. In the genetic algorithm, long computation times are the consequence of the high number of filter calculations that need to be performed in each generation. This is directly related to the population size. A smaller population size could be used to speed up the optimisation, although this would reduce the variety in candidate solutions. Another way to reduce computation time in future, is by using a modified initial population. If the algorithm has already been used for several cases, optimal filter compositions can be stored. In new cases, part of the initial population could be composed of the previously obtained solutions instead of random solutions. This would probably improve the starting position of the algorithm and reduce the number of generations that is needed to find an optimum.

# 8 Conclusion

## 8.1 Concluding remarks on the model problem

Two types of algorithms have been applied on the model problem. In these optimisations, several filter configurations were found that led to comparable dose distributions in the brain phantom. In the resulting treatment plans, a sufficiently high mean tumour dose could be delivered within a total treatment time of 3 to 6 hours, while the maximum dose in the OAR stayed far below the imposed dose constraint. However, none of the treatment plans succeeded in delivering a sufficiently uniform dose distribution inside the tumour. Even in the best found solution, dose values between 75% and 118% of the prescribed dose were present in the tumour. These unsatisfactory outcomes are probably due to the combination of the limited number of allowed beam directions, the large tumour size and maybe most importantly, the fact that the tumour touches the OAR. As a consequence, it seems almost impossible or at least difficult to set up an effective BNCT treatment plan for this specific case. It appears that a combination of BNCT and photon therapy is able to provide better dose distributions in this case, which became clear from the absence of gamma shields in most of the optimised filter compositions. In the best solution, almost one fifth of the total tumour dose was delivered by gammas that were present in the neutron beams.

An increase of the $^{10}$B uptake ratio between the tumour and healthy tissue is not expected to improve the result in this specific case, since this would not influence the dose uniformity within the tumour. However, there are some other simple modifications that could be implemented to improve the best possible outcome of the model problem. First of all, one could increase the voxel weights in the tumour region. This would probably lead to a higher dose in the OAR, which is still permitted by the current dose constraint. A further improvement could be obtained by irradiating the tumour from different angles. Additional neutron beams could be added orthogonal to the $xy$-plane. It is also suggested to adjust the objective function by penalising for long treatment times. This would result in a better balance between the beam quality and intensity in the optimised configuration.

The geometrical description in the model problem is obviously an extremely simplified representation of the human brain. In future work, the optimisation methods should be tested for more realistic cases. This could be done by using CT or MRI data from real patients to determine the tissue compositions. Also, the micro-distribution of the boron compounds should be modelled more accurately. MCNP is not suitable for using such a detailed geometry description. Therefore, an alternative transport code is needed to calculate the dose transfer matrices.

## 8.2 General conclusions

First of all, a transport model was developed based on iterative multiplication of transmission and reflection matrices. This model has been useful in performing fast transport calculations in neutron filters. A significant reduction in computation time was accomplished by this method compared to discrete ordinates calculations in XSDRN. The use of sparse matrices was of little additional benefit. There could be possibilities to use this transport model in other applications, such as shielding problems. Basically all coupled neutron-gamma transport calculations in slab geometries are applicable.

In this thesis, the transmission and reflection matrices were calculated in XSDRN. This has resulted in some inaccuracies. In XSDRN, the filter geometry is approximated by a one-dimensional model. This means that the effect of particles leaking away in the radial direction is not taken into account. Furthermore, a few negative values appeared in the transmission matrices, which were assumed to be caused by extrapolation errors in XSDRN. Although this effect was not large, these values were not in agreement with physically possible neutron fluxes. For future applications, it is recommended to calculate the matrix elements by Monte Carlo simulations. This method enables the possibility to take leakage into account and the resulting output fluxes are guaranteed to be positive. The increase in computation time is acceptable since each slab needs to be simulated only once, after which the matrices are stored for future use.

The largest part of this work was focused on the optimisation of neutron filters. Two types of algorithms were developed for this purpose. Both the gradient-based algorithm and the genetic algorithm have shown to be capable of finding effective neutron filters. In both methods it seems impossible to tell if a global minimum was found. However, this is not always necessary in practice; a local optimum could be sufficient provided that the treatment plan satisfies its requirements. Several optimisation runs have demonstrated the large variety in optimised filter compositions. Depending on the starting point or initial population, completely different solutions can be found that produce similar dose distributions.

Both optimisation methods require approximately the same amount of computation time. About one or two days were needed to find a solution if the calculations were performed on 5 cores. In addition to that, the dose transfer matrices had to be calculated beforehand. This also took several days up to one week depending on the number of allowed beam directions. All together, this adds up to relatively long calculations that need to be performed for each individual patient. Additional work is necessary to achieve a reduction in computation time. In both algorithms, there seem to be possibilities to realize this. In the gradient descent algorithm, it would be interesting to investigate if stochastic gradient descent could be applied [52]. In the genetic algorithm, one could experiment with varying optimisation parameters and using a newly defined initial population.

Once the optimised filter compositions are determined, some additional steps are required to realize the components in practice. Especially for the filters obtained by the gradient descent algorithm, this could cause some difficulties because of the continuous filter model. The mixed layers were defined as a theoretical concept, but there are several ways to approximate them in practice. One of the possibilities is to use a combination of thin alternating layers which resembles the characteristics of a mixture. It might take too much effort to build a new neutron filter for every patient and perhaps this is not even necessary, assuming that the same neutron filter can be applied in similar cases. It would be useful to design various filters that are optimised for different tumour sizes and depths. This way, a set of neutron filters could be created that is usable in a wide range of cases.

The future of BNCT depends on many different aspects, such as the development of more selective boron compounds and the availability of accelerator-based neutron sources. If progress is made in these areas, BNCT could become a serious alternative for other cancer treatments. The optimisation methods in this work could serve as a tool to design neutron filters for future BNCT applications.

# A | Specification of the Filter Layers

Table A.1 contains the characteristics of the filter layers that were used in the optimisations. For each layer, the thickness $\Delta x$ and mass density $\rho$ are given. Also, the nuclides with their atomic fractions are specified. In some layers, this corresponds to the natural abundance of the isotopes. Other materials are purely composed of a single nuclide that possesses some useful properties.

**Table A.1:** Specifications of the filter layers that were used in all optimisations.

| **Material** | **$\Delta x$ (cm)** | **$\rho$ (g/cm$^3$)** | **Nuclide** | **Atomic %** |
|---|---|---|---|---|
| Al | 10 | 2.70 | Al-27 | 100.0 |
| Si | 10 | 2.33 | Si-28 | 100.0 |
| S | 10 | 2.07 | S-32 | 100.0 |
| Mg | 6 | 1.74 | Mg-24 | 79.0 |
| | | | Mg-25 | 10.0 |
| | | | Mg-26 | 11.0 |
| $AlF_3$ | 5 | 3.10 | F-19 | 300.0 |
| | | | Al-27 | 100.0 |
| LiF | 5 | 2.64 | Li-7 | 100.0 |
| | | | F-19 | 100.0 |
| Bi | 4 | 9.80 | Bi-209 | 100.0 |
| Pb | 3 | 11.34 | Pb-204 | 1.4 |
| | | | Pb-206 | 24.1 |
| | | | Pb-207 | 22.1 |
| | | | Pb-208 | 52.4 |
| Ti | 2 | 4.50 | Ti-46 | 100.0 |
| Ni | 0.5 | 8.90 | Ni-60 | 100.0 |
| $B_4C$ | 0.02 | 2.52 | B-10 | 79.6 |
| | | | B-11 | 320.4 |
| | | | C-12 | 98.9 |
| | | | C-13 | 1.1 |
| Cd | 0.02 | 8.64 | Cd-106 | 1.3 |
| | | | Cd-108 | 0.9 |
| | | | Cd-110 | 12.5 |
| | | | Cd-111 | 12.8 |
| | | | Cd-112 | 24.1 |
| | | | Cd-113 | 12.2 |
| | | | Cd-114 | 28.7 |
| | | | Cd-116 | 7.5 |

# B | Transport Calculations in XSDRN

The transmission and reflection matrices of all filter layers have been calculated in XSDRN. Each matrix column is the result of a single calculation for a given unit source with a specific energy and angle. Before the transport calculations are performed in XSDRN, the group cross sections need to be determined by CSASI. This is another module in the larger SCALE Code System [33].

The input files for these calculations are written using the FIDO format. The XSDRN input data is divided over five data blocks. All data blocks are composed of cards in which the input variables are specified. The general problem description is inserted in the first input card. The most relevant fields of this card are included in Table B.1.

**Table B.1:** Relevant fields in the first input card of XSDRN which are used to define the general problem description.

| Field | Variable | Value | Description |
|---|---|---|---|
| 1 | IGE | 1 | slab geometry |
| 2 | IZM | 1 | number of separate material zones |
| 3 | IM | 101 | number of spatial intervals |
| 4 | IBL | 0 | vacuum boundary condition at the left-hand boundary of the system |
| 5 | IBR | 0 | vacuum boundary condition at the right-hand boundary of the system |
| 8 | ISN | 16 | the order of angular quadrature |
| 9 | ISCT | 5 | the order of scattering |
| 10 | IEVT | 0 | fixed source calculation |
| 14 | ITH | 0 | solve the forward Boltzmann equation |

As an example, one of the input files is given below. This file was used to perform the transport calculation in a 4 cm thick layer of bismuth. The fixed source emits neutrons in the first energy group ($g = 1$) in the most forward angular direction ($m = 16$). Some comments were added for further explanations:

---

```
=csasi parm=centrm                          % CSASI is used to calculate the
LOAD CROSS SECTIONS                         % group cross sections
V7.1—200N47G                                % Energy groups library
read comp                                   % Material composition
Bi 1 END                                    % Material 1 = bismuth
end comp
end data
end
=shell
mv ft02f001 $RTNDIR/xs.out
end
=shell
ln —fs $RTNDIR/xs.out ft04f001
end
```

```
=xsdrn
TRANSPORT CALCULATION
1$$ 1 1 101 0 0 1 1 16 5 0 250 250 0 0 e    % (See Table B.1)
3$$ 0 0 1 a8 1 e                            % Field 8 is used to read in 38**
5** 1e-4 1e-5 e 1t                          % Convergence criteria
13$$ 1                                      % Mixing table
14$$ 1                                      %
15** 1 2t                                   %
30$$ 1 f0                                   % Source at first interval
32** 16r0 1 f0 3t                           % Source spectrum
33## f0 4t                                  % Initial flux guess
35** -1 99i 0 4.000 e                       % Interval boundaries
36$$ 101r1 e                                % Zone number per interval
38** 0 100r1 e                              % Density factor per interval
39$$ 1 e 5t                                 % Mixture number by zone
end
=shell
cp ft16f001 $RTNDIR/flux_ang.out
end
```

# C | The Genetic Algorithm

This section contains a complete description of the genetic algorithm that was used to optimise the filter compositions. The algorithm is based on the documentation of the *ga* function from the Global Optimisation Toolbox of Matlab. Some modifications have been applied to enable the combination of using integer variables and customized crossover and mutation functions.

First, the optimisation parameters and solution variables are specified:

```
GA.nvars = 125;                     % Number of variables
GA.maxint = 12;                     % Maximum value for variables
GA.NoG = 250;                       % Number of generations
GA.PS = 200;                        % Population size
GA.EC = round(0.05*GA.PS);          % Elite count (5% of population size)
GA.TS = 4;                          % Tournament size
GA.COP = 0.8;                       % Crossover probability
GA.MP = 1 - GA.COP;                 % Mutation probability

population = zeros(GA.PS,GA.nvars); % Rows represent solutions in current population
score = zeros(GA.PS,GA.NoG);        % Element (i,j) gives score of solution i
                                      in generation j
```

In the first generation, an initial population is generated and the objective function is evaluated for each individual. This objective is defined as a function of the filter composition `x`, the input spectrum `phi_in`, transmission and reflection matrices `T` and `R`, the dose transfer matrices `wd` and the phantom description `geo`.

```
gen = 1;                                              % First generation
population = randi([0,GA.maxint],size(population)); % Create initial population
for p=1:GA.PS
    x = population(p,:);                              % Select current solution
    score(p,gen) = objective(x,phi_in,T,R,wd,geo);   % Evaluate objective function
end
gen = gen + 1;
```

The evolution of the further generations proceeds as follows:

```
while gen <= GA.NoG
    newpop = zeros(GA.PS,GA.nvars);                 % Create new empty population
    [~,ind.elite] = mink(score(:,gen−1),GA.EC);     % Select elite solutions
    newpop(1:GA.EC,:) = population(ind.elite,:);    % Copy elite solutions
    score(1:GA.EC,gen) = score(ind.elite,gen−1);    % Copy elite scores

    for p=(GA.EC+1):2:GA.PS
        ind.par1 = tournament(score(:,gen−1),GA);   % Select parent solutions
        ind.par2 = tournament(score(:,gen−1),GA);
        if rand(1) < GA.COP                         % Create new solutions
            [newpop(p,:),newpop(p+1,:)] = ...
                crossover(population(ind.par1,:),population(ind.par2,:),GA);
        else
            [newpop(p,:),newpop(p+1,:)] = ...
                mutation(population(ind.par1,:),population(ind.par2,:),GA);
        end
    end

    population = newpop; clear newpop;              % Replace old by new population
    for p=(GA.EC+1):GA.PS
        x = population(p,:);
        score(p,gen) = objective(x,phi_in,T,R,wd,geo);
    end
    gen = gen + 1;
end
```

The crossover and mutation operation are given by the following functions:

```
function [child1,child2] = crossover(parent1,parent2,GA)
selection = randperm(GA.nvars,round(GA.nvars/2));
bin = zeros(1,GA.nvars);
bin(selection) = 1;
child1 = bin.*parent1 + (1−bin).*parent2;
child2 = (1−bin).*parent1 + bin.*parent2;
end
```

```
function [child1,child2] = mutation(parent1,parent2,GA)
frac = 0.1;     % mutation fraction
selection = randperm(GA.nvars,round(frac*GA.nvars));
child1 = parent1;
child1(selection) = randi([0,GA.maxint],1,round(frac*GA.nvars));
selection = randperm(GA.nvars,round(frac*GA.nvars));
child2 = parent2;
child2(selection) = randi([0,GA.maxint],1,round(frac*GA.nvars));
end
```

# Bibliography

[1] Rolf F Barth, Jeffrey A Coderre, M Graça H Vicente, and Thomas E Blue. Boron neutron capture therapy of cancer: current status and future prospects. *Clinical Cancer Research*, 11(11):3987–4002, 2005.

[2] Wolfgang AG Sauerwein, Andrea Wittig, Raymond Moss, and Yoshinobu Nakagawa. *Neutron capture therapy: principles and applications*. Springer Science & Business Media, 2012.

[3] Nuclear Energy Agency. *Nuclear Data Sheets*, volume 112, 2011.

[4] G L Locher. Biological effects and therapeutic possibilities of neutrons. *Am. J. Roentgenol. Radium Ther.*, 36:1–13, 1936.

[5] P Gerald Kruger. Some biological effects of nuclear disintegration products on neoplastic tissue. *Proceedings of the National Academy of Sciences of the United States of America*, 26(3):181, 1940.

[6] Paul A Zahl and Franklin S Cooper. Localization of lithium in tumor tissue as a basis for slow neutron therapy. *Science*, 93(2403):64–65, 1941.

[7] James J Vredenburgh, Annick Desjardins, James E Herndon, Jennifer Marcello, David A Reardon, Jennifer A Quinn, Jeremy N Rich, Sith Sathornsumetee, Sridharan Gururangan, John Sampson, et al. Bevacizumab plus irinotecan in recurrent glioblastoma multiforme. *Journal of clinical oncology*, 25(30):4722–4729, 2007.

[8] International Atomic Eenergy Agency. Current status of neutron capture therapy. Technical report, IAEA-TECDOC-1223. Vienna, 2001.

[9] Daniel N Slatkin. A history of boron neutron capture therapy of brain tumours: postulation of a brain radiation dose tolerance limit. *Brain*, 114(4):1609–1629, 1991.

[10] Hiroshi Hatanaka. Boron neutron capture therapy for tumors. *International Journal of Radiation Applications and Instrumentation. Part A. Applied Radiation and Isotopes*, 37(1):79–80, 1986.

[11] WH Sweet. Medical aspects of boron-slow neutron capture therapy. Technical report, 1986.

[12] AH Soloway, H Hatanaka, and MA Davis. Penetration of brain and brain tumor. vii. tumor-binding sulfhydryl boron compounds. *Journal of medicinal chemistry*, 10(4):714–717, 1967.

[13] Y Mishima, M Ichihashi, S Hatta, Ch Honda, K Yamamura, T Nakagawa, H Obara, J Shirakawa, J Hiratsuka, K Taniyama, et al. First human clinical trial of melanoma neutron capture. diagnosis and therapy. *Strahlentherapie und Onkologie*, 165(2/3):251–254, 1989.

[14] Raymond L Moss. Critical review, with an optimistic outlook, on boron neutron capture therapy (BNCT). *Applied Radiation and Isotopes*, 88:2–11, 2014.

[15] L Kankaanranta, H Koivunoro, M Kortesniemi, P Välimäki, T Seppälä, P Kotiluoto, I Auterinen, M Kouri, S Savolainen, H Joensuu, et al. Bpa-based bnct in the treatment of glioblastoma multiforme: A dose escalation study. In *13th International Congress on Neutron Capture Therapy, A New Option Against Cancer; November 2–7; Florence, Italy*, 2008.

[16] Rolf F Barth, Albert H Soloway, Ralph G Fairchild, and Robert M Brugger. Boron neutron capture therapy for cancer. realities and prospects. *Cancer*, 70(12):2995–3007, 1992.

[17] Hiroyuki Nakamura and Mitsunori Kirihata. Boron compounds: new candidates for boron carriers in bnct. In *Neutron capture therapy*, pages 99–116. Springer, 2012.

[18] Yukio Nagasaki, Shogo Sumitani, Motoi Oishi, Tatsuya Yaguchi, Hiroki Murotani, Yukichi Horiguchi, Minoru Suzuki, Koji Ono, and Hironobu Yanagie. Design of boron-containing nanoparticle for high performance bnct. In *15th International Congress on Neutron Capture Therapy, Tsukuba, Japan, September*, pages 10–14, 2012.

[19] Andres J Kreiner. Accelerator-based bnct. In *Neutron Capture Therapy*, pages 41–54. Springer, 2012.

[20] DR White, HQ Woodard, and SM Hammond. Average soft-tissue and bone models for use in radiation dosimetry. *The British journal of radiology*, 60(717):907–913, 1987.

[21] AM Hassanein, MH Hassan, Nader MA Mohamed, and MA Abou Mandour. An optimized epithermal bnct beam design for research reactors. *Progress in Nuclear Energy*, 106:455–464, 2018.

[22] D Ross, G Constantine, DR Weaver, and TD Beynon. Designing an epithermal neutron beam for boron neutron capture therapy for a dido type reactor using mcnp. *Nuclear Instruments and Methods in Physics Research Section A: Accelerators, Spectrometers, Detectors and Associated Equipment*, 334(2-3):596–606, 1993.

[23] G Tracz, L Dabkowski, D Dworak, K Pytel, and U Woźnicka. The filter/moderator arrangement–optimisation for the boron–neutron capture therapy (bnct). *Radiation protection dosimetry*, 110(1-4):827–831, 2004.

[24] M Azahra, A Kamili, H Boukhal, et al. Monte carlo calculation for the development of a bnct neutron source (1 ev–10 kev) using mcnp code. *Cancer/Radiotherapie*, 12(5):360–364, 2008.

[25] Henry T Motz. Slow-neutron capture gamma rays from sodium and cadmium. *Physical Review*, 104(5):1353, 1956.

[26] Bob D'Mellow, David J Thomas, Malcolm J Joyce, Peter Kolkowski, Neil J Roberts, and Stephen D Monk. The replacement of cadmium as a thermal neutron filter. *Nuclear Instruments and Methods in Physics Research Section A: Accelerators, Spectrometers, Detectors and Associated Equipment*, 577(3):690–695, 2007.

[27] JH Hubbell. Photon mass attenuation and energy-absorption coefficients. *The International Journal of Applied Radiation and Isotopes*, 33(11):1269–1290, 1982.

[28] Narveer Singh, Kanwar Jit Singh, Kulwant Singh, and Harvinder Singh. Comparative study of lead borate and bismuth lead borate glass systems as gamma-radiation shielding materials. *Nuclear Instruments and Methods in Physics Research Section B: Beam Interactions with Materials and Atoms*, 225(3):305–309, 2004.

[29] Robert M Fink. Biological studies with polonium, radium, and plutonium, 1950.

[30] JJ Duderstadt and LJ Hamilton. *Nuclear Reactor Analysis.* John Wiley and Sons, 1976.

[31] Bradley T Rearden and Matthew Anderson Jessee. Scale code system. Technical report, Oak Ridge National Lab.(ORNL), Oak Ridge, TN (United States), 2018.

[32] BG Carlson and KD Lathrop. Discrete ordinates angular quadrature of the neutron transport equation. *LA-3186, Los Alamos National Laboratory*, 1965.

[33] B.T. Rearden M.A. Jessee. *SCALE Code System.* Oak Ridge National Laboratory, 6 edition, 3 2018.

[34] DH Wilkinson. Nuclear photodisintegration. *Physica*, 22(6-12):1039–1061, 1956.

[35] D Feilzer. Gd-PSMA neutron capture therapy. A computational feasibility and method development study. Master's thesis, Delft University of Technology, 9 2018.

[36] T Goorley, M James, Thomas Booth, F Brown, J Bull, LJ Cox, J Durkee, J Elson, Michael Fensin, RA Forster, et al. Initial mcnp6 release overview. *Nuclear Technology*, 180(3):298–315, 2012.

[37] Gayane Abdullaeva, Gulnara Djuraeva, Andrey Kim, Yuriy Koblik, Gairatulla Kulabdullaev, Turdimukhammad Rakhmonov, and Shavkat Saytjanov. Evaluation of absorbed dose in gadolinium neutron capture therapy. *Open Physics*, 13(1), 2015.

[38] VA Nievaart. *Spectral Tailoring for Boron Neutron Capture Therapy.* PhD thesis, Delft University of Technology, 6 2007.

[39] N Gupta, RA Gahbauer, TE Blue, and B Albertson. Common challenges and problems in clinical trials of boron neutron capture therapy of brain tumors. *Journal of neuro-oncology*, 62(1):197–210, 2003.

[40] David W Nigg. Computational dosimetry and treatment planning considerations for neutron capture therapy. *Journal of neuro-oncology*, 62(1):75–86, 2003.

[41] Faezeh Rahmani and Majid Shahriari. Beam shaping assembly optimization of linac based bnct and in-phantom depth dose distribution analysis of brain tumors for verification of a beam model. *Annals of Nuclear Energy*, 38(2-3):404–409, 2011.

[42] Jérôme Maurice Verbeke. Development of high-intensity DD and DT neutron sources and neutron filters for medical and industrial applications. Technical report, Lawrence Berkeley National Lab.(LBNL), Berkeley, CA (United States), 2000.

[43] Silvia Scoccianti, Beatrice Detti, Davide Gadda, Daniela Greto, Ilaria Furfaro, Fiammetta Meacci, Gabriele Simontacchi, Lucia Di Brina, Pierluigi Bonomo, Irene Giacomelli, et al. Organs at risk in the brain and their dose-constraints in adults and in children: a radiation oncologist's guide for delineation in everyday practice. *Radiotherapy and Oncology*, 114(2):230–238, 2015.

[44] Jinyu Xue, H Warren Goldman, Jimm Grimm, Tamara LaCouture, Yan Chen, Lesley Hughes, and Ellen Yorke. Dose-volume effects on brainstem dose tolerance in radiosurgery. *Journal of neurosurgery*, 117(Special_Suppl):189–196, 2012.

[45] RL Moss, F Stecher-Rasmussen, K Ravensberg, G Constantine, and P Watkins. Design, construction and installation of an epithermal neutron beam for bnct at the high flux reactor petten. In *Progress in neutron capture therapy for cancer*, pages 63–66. Springer, 1992.

[46] AR Groenhof, AAR Wetzel, and HT Wolterbeek. Reactor institute delft. *Atw. Internationale Zeitschrift fuer Kernenergie*, 58(10):608–610, 2012.

[47] Bernard Ponsard, SC Srivastava, LF Mausner, FF Russ Knapp, MA Garland, and S Mirzadeh. Production of sn-117m in the br2 high-flux reactor. *Applied Radiation and Isotopes*, 67(7-8):1158–1161, 2009.

[48] Randy L Haupt and Sue Ellen Haupt. Practical genetic algorithms. 2004.

[49] Kusum Deep, Krishna Pratap Singh, Mitthan Lal Kansal, and C Mohan. A real coded genetic algorithm for solving integer and mixed integer optimization problems. *Applied Mathematics and Computation*, 212(2):505–518, 2009.

[50] Michael Negnevitsky. *Artificial intelligence: a guide to intelligent systems.* Pearson education, 2005.

[51] Melanie Mitchell, James P Crutchfield, Rajarshi Das, et al. Evolving cellular automata with genetic algorithms: A review of recent work. In *Proceedings of the First International Conference on Evolutionary Computation and Its Applications (EvCA'96)*, volume 8. Moscow, 1996.

[52] Tong Zhang. Solving large scale linear prediction problems using stochastic gradient descent algorithms. In *Proceedings of the twenty-first international conference on Machine learning*, page 116. ACM, 2004.